Multiscale Modeling of Oil Uptake in Fried Products

Jean-Michaël Vauvre
INRA, UMR 1145 Ingénierie Procédés Alimentaires, Group Interaction between Materials and Media in Contact, F-91300 Massy, France

AgroParisTech, UMR 1145 Ingénierie Procédés Alimentaires, F-91300 Massy, France

McCain Alimentaire S.A.S., Parc d'entreprises de la Motte du Bois, 62440 Harnes, France

Anna Patsioura and Vitrac Olivier
INRA, UMR 1145 Ingénierie Procédés Alimentaires, Group Interaction between Materials and Media in Contact, F-91300 Massy, France

AgroParisTech, UMR 1145 Ingénierie Procédés Alimentaires, F-91300 Massy, France

Régis Kesteloot
Régis Kesteloot conseil, 60 Avenue du Colonel Driant, 59130 Lambersart, France

DOI 10.1002/aic.14801
Published online April 8, 2015 in Wiley Online Library (wileyonlinelibrary.com)

Oil–air biphasic flow has been simulated at the scale of an entire potato tuber tissue using a Kinetic Monte-Carlo (KMC) formulation parameterized on microscopic observations. Extrapolations to more general configurations are proposed by combining the proposed KMC framework with oil momentum equations integrated at microscopic scale. Branched percolation routes in three-dimensional honeycomb arrangement of cells are explored using a first-passage algorithm. Three major applications are presented. KMC simulations are first considered to homogenize sparse dynamic observations at the scale of isolated cells up to the scale of a full tissue. The second application investigates the effect of cell damages on oil uptake. Finally, our general KMC formulation was successfully compared with a diffusive model of oil uptake. Comprehensive rules to set the distribution parameters of all quantities (kinetic and structure parameters) from scarce observations or general assumptions are discussed. © 2015 American Institute of Chemical Engineers *AIChE J*, 61: 2329–2353, 2015

Keywords: porous media, spontaneous imbibition, percolation model, kinetic Monte-Carlo, deep-frying

Introduction

It is generally accepted that oil penetrates inside a fried product once the product is removed from the oil bath.[1,2] Several physical models have been proposed to describe oil uptake in post-frying conditions in fried products as reviewed in Refs. 2–7. They fall into four categories: phenomenological models,[8] mechanistic models based on conversion laws in an effective medium,[9–11] stochastic percolation models,[12,13] and capillary models.[14–16] Despite increasing sophistications in the number of coupling in post-frying conditions (heat transfer, steam condensation, water liquid transport), all proposed models fail to predict oil uptake in products as common as potato French-fries or potato chips. They must be thought as attempts to test the consistency of physical assumptions rather than as predictive models with a practical use for the industry. Previous descriptions are insufficient, mainly because they do not incorporate the important details such as the organization of the cellular network, the state of cells (emptied, filled with molten or native starch) and the localization of ruptures. Oil uptake is indeed a local phenomenon and not a macroscopic one: only empty cells connected to others through defects can be filled with oil.[17,18] As the dry region in fried products (so-called crust) is only few cells thick (from 3 to 6), the permeability of the fried tissue cannot be consistently homogenized laterally, averaged across the thickness and finally tabulated regardless the potato variety, the process condition, and the direction of cut. Hence, the connectivity of cells is strongly affected by the whole product hydrothermal history.[19] In addition, the possible biphasic nature of oil–air uptake in post-frying conditions can make oil penetration dynamics more heterogeneous,[20] deviating significantly from the fractional flow analysis of Bucklet-Leverett.[21]

Very recently, a first experimental observation of the displacement of oil–air front in the crust[22] highlighted two important results: oil capillary rise is proportional to the square root of time—consistently with the Lucas–Washburn equation—but much slower than it could be thought from the apparent size of capillaries. In particular, the

Additional Supporting Information may be found in the online version of this article.

Correspondence concerning this article should be addressed to O. Vitrac at olivier.vitrac@agroparistech.fr.

© 2015 American Institute of Chemical Engineers

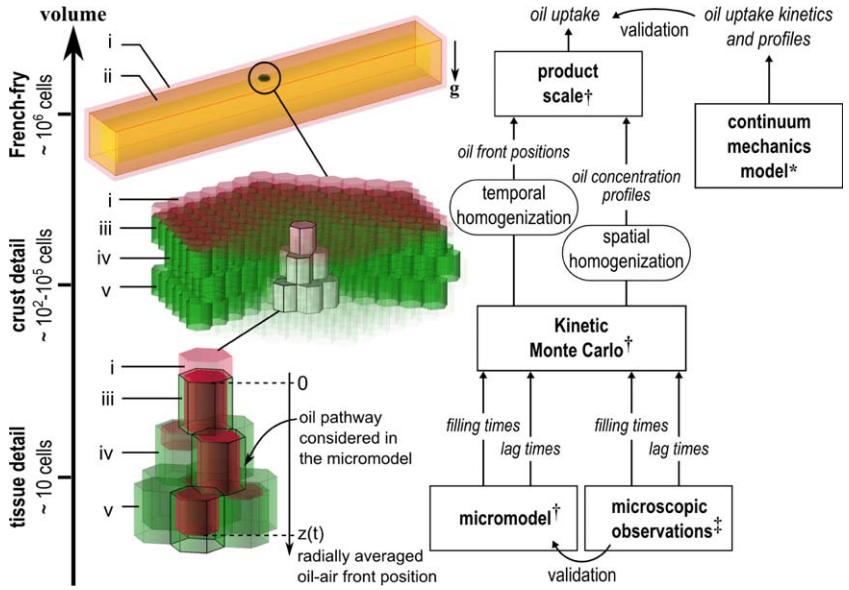

Figure 1. Coupled simulation scales to describe oil uptake in a typical fried product such as French-fries: (1) oil adhering to the surface; (2) dried potato crust; (3) first cell layer; (4) second cell layer; (5) third cell layer.

† this work; ‡dynamic microscopic observations from Ref. 20; *continuum mechanics simulations of Ref. 11. [Color figure can be viewed in the online issue, which is available at wileyonlinelibrary.com.]

displacement rates were found about 15 times slower than the values predicted by the Lucas–Washburn type equation. We corroborated recently the previous results on lengthwise-cut potato crusts by observing directly the dynamics of oil percolation at cellular scale in simulated post-frying conditions.[20] The first cell layer was shown to be almost instantaneously filled with oil, whereas oil percolation from one cell to the next one was strongly delayed due to the presence of trapped air bubbles. Retardations in connected porous networks are well established in porous media.[23–25] They are connected to both immiscible fluid displacements and to convergent-divergent configurations.[26,27]

The main goal of this work is to elucidate the contribution of (1) the size of defects connecting cells and (2) the presence of trapped air on oil percolation dynamics and, finally, on oil uptake. The complications arise from the large variety of air escape mechanisms at cellular scale, from the random nature of cellular defects,[18] and from the broad distribution of time scales, ranging from 10^{-1} s to 10^{4} s according to experimental observations.[20] This work shows that the lower bound could be even as low as 10^{-4} s. As one single French-fry ($100 \times 9 \times 9$ mm^3) consists in approximately 10^6 cells, simulating oil percolation at cellular scale is very challenging. The dimension of the problem can be slightly reduced by noticing that oil invasion occurs mainly in the dry crust surrounding the product. With a thickness varying from 2 to 6 cell layers, the crust in a single potato strip represents between 8×10^4 and 2×10^5 cells. During the last decade, several meshless techniques have been devised or adapted to simulate multiphase flows in porous media at microscopic scale.[28] They include: adhesive dissipative particle dynamics,[29] smooth particle hydrodynamics,[30] lattice Boltzmann methods modified to account for solid adhesion and fluid cohesion,[31–34] front tracking/capturing methods,[35,36] volume-of-fluid methods.[37] Their primary motivation is usually to preserve sharp interfaces and to describe the dynamics of fluid phase fragmentation. According to considered ground details, they fit better for pore scale modeling (e.g., oil flow through cell wall defects) than for simulating the long-time evolution of a wetting phase in large cellular systems. As reported in Ref. 38 and in references herein, the chief difficulty in spontaneous imbibition arises from the filling sequence of pores while simulating dynamically all details of flows and swelling layers. In this article, we propose to circumvent the difficulty by applying to a two-scale modeling approach as illustrated in Figure 1.

At the largest scale, the potato tissue or crust, the displacements of many oil–air menisci across random defects is described stochastically as a collection of independent Poissonian events (macromodel). This description is consistent with our dynamic observations at microscopic scale[20] and can be efficiently simulated using Kinetic Monte-Carlo (KMC) methodology. Although event-driven KMC schemes can manage transitions spread over a broad range of time scales,[39–41] they suffer important limitations. In particular, they require the transition rates or dwelling times to be known. As our initial set of experimental data covered only filling and first-passage times for two-cell layers-thick potato tissue in presence of low damage ratios, a micromodel has been alternatively devised at cellular scale. Inspired by the abundant literature on spontaneous liquid imbibition in capillary tubes and networks (see reviews in Refs. 38,42,43), our choice was oriented to a phase-averaged formulation instead of a volume-averaged one (see the distinction in Refs. 44,45). It offers the advantages of keeping the fractal nature of the oil-gas interface,[46,47] which could be compared with microscopic observations. Four important constraints were explicitly considered: (1) the threshold of percolation in honeycomb structures,[48,49] (2) the immiscible displacement of air and oil,[50,51] (3) the presence of buoyancy forces,[52–54] (4) the pressure ahead the oil meniscus.[55–59] By reusing several concepts previously devised to describe diffusive phenomena at supramolecular scale[60] or to solve transport equations when all parameters are known

by their distributions,[61] we show that the distributions of filling times and first-passage times can be parametrized from the main physical quantities (number of layers, size of defects, presence of air, etc.). For practical applications (French-fries, chips…), we demonstrate, without a loss of generality, that their distributions can be efficiently approximated by Gamma ones and that their parameters can be inferred by recurrence.

The article is organized as follows. The micromodel is introduced in section two by integrating oil momentum equations along an arbitrary curvilinear piecewise capillary. The combined effects of section changes and of air flow configurations are illustrated. It is shown that the complex dynamics of oil percolation between cells through defects, with or without trapped bubbles, led to separable events and can be essentially captured through two numbers: a filling time and a lag-time (or equivalently a first-time passage). As their first moments and their distribution in values can be obtained by recurrence when oil passes n constrictions, the previous results on simple arrangements can be generalized to branched configurations. Section three details the KMC methodology followed to simulate oil imbibition at the scale of the potato crust. Section four presents the whole approach on several situations with general interest: oil uptake in tissues initially filled with air, biological materials subjected to gradients of damage and one comparison with the deterministic mechanistic model of Ref. 10. The main findings and general recommendations are finally summarized in section five.

Theory

Background

Details on the thermodynamic conditions met during immersion frying and immediately after frying can be found in Refs. 3,19,62 and in the theoretical section of Ref. 20, respectively. When the fried product is removed from the oil bath, the composition of the gas phase filling cells evolve from pure steam to a humid air mixture. According to the rate of incorporation of cold air, the replacement of steam by air can be followed by a substantial negative pressure gauge. In absence of steam condensation (no significant pressure gauge), observations of Ref. 20 showed that the spontaneous oil imbibition of a parenchyma honeycomb structure initially filled by air and without starch obeys mainly to a restricted oil–air counter-current flow. Counter-current configurations dominate when one single end-face surface participates to mass transfer and when air cannot escape by crossing cell walls. Co-current configurations occur when air can escape through throats (e.g., defects) different from those used by oil to penetrate the cells. In both cases, the main driving force is the capillary pressure generated by the curved interfaces along walls, possibly augmented with gravity. Similar multiphase mechanisms of liquid infiltration have been described in many engineering problems involving various porous media: paper coatings,[63] powders,[64] soil,[65] rocks,[66] and so forth. They show all a strong oil infiltration reduction and slowdown when the displacement of air is hampered. The microscopic details of the slip between fluid phases have been more specifically studied in simple configurations with many-body dissipative particle dynamics simulations.[67,68] Using analogies with oil recovery in fractured reservoirs,[69,70] oil penetration in an effective channel with an hydraulic radius r and length $L_{\max}$, is expected to be roughly homothetic respectively to the following dimensionless time Fo_C (so-called capillary "Fourier number")

$$Fo_C = \frac{\gamma r t}{f(\eta_{oil}, \phi_{air}, \text{geometry}) L_{\max}^2} \quad (1)$$

where t is time, γ is the oil–air surface tension and $f()$ is an effective viscosity increasing in a non-trivial manner with the dynamic viscosity of oil, η_{oil}, the volume fraction of air and the number of constrictions. In presence of long or large channels and in presence of large air fraction, oil imbibition is expected to require longer times. In presence of strong negative pressure gauge provoked by steam condensation, oil percolation is expected, conversely, to be dramatically faster and governed by forced imbibition. In addition, recent observations of oil penetration in connected microchannels showed that oil uptake could be reduced from 95% down to 9% when air was enabled to percolate in competition with oil.[71] This section proposes a general micromodel to explain the mentioned experimental facts and to infer the rate constants required by the KMC simulation scheme detailed in section "Materials and Methods." The phase-averaged formulation uses the position of the oil–air front,z, as state variable within a skewed oil pathway defined by the positions of adjacent cells connected through cell wall defects, as shown in Figure 1. This position should be envisioned as radially-averaged at cellular scale.

Micromodel of oil uptake at cellular scale

Oil Transport. Because oil percolates mainly through defects (or "throats") occurring at end junctions of cells (see Figure 2a), oil seems to infiltrate skewed capillaries, whose turns are set by the arrangement of cells and the connectivity of defects. The displacement of a liquid meniscus at the gas–liquid interface within a capillary of arbitrary shape and length has been first described using a phase-averaged approach by BeMiller and Whistler[72] and independently by Washburn.[73] During the last decade, their equation has been reviewed and extended by several authors[56,74] but mainly for capillaries with uniform cross-sections. The effects of axial variations of cross-sections on the displacement of the liquid-gas front have been specifically addressed by Reyssat et al.[75] Regardless the true shape of the meniscus, all models assume a Poiseuille flow along the majority of the penetrated distance z (i.e., far from the entrance and meniscus). Without a loss of generality, oil penetration route can be assumed to be axisymmetric with a radius $r(\zeta)$ at position $\zeta > 0$ so that the radial average velocity $v(\zeta)$ is proportional to the local pressure drop as

$$v(\zeta) = -\frac{r_{(\zeta)}^2}{8\eta} \frac{dP}{dz}\Big|_{(\zeta)} \quad (2)$$

Oil penetration routes through parenchyma cells can be consistently approximated as connected capillaries with sections varying between the radius of an empty cell and the radius of defects between cells as illustrated in Figure 2. In this work, the variations of flow rate due to the variations of the cross-sections are explicitly considered by assuming piecewise variations of the cross-sections. The equivalent radii appearing in this theoretical section are therefore defined as hydraulic radii (i.e., ratio of the cross-section of the oil flow to its wetted perimeter). This definition preserves the shear stress at the walls in hexagonal parenchyma cells comparatively to their cylindrical idealization.

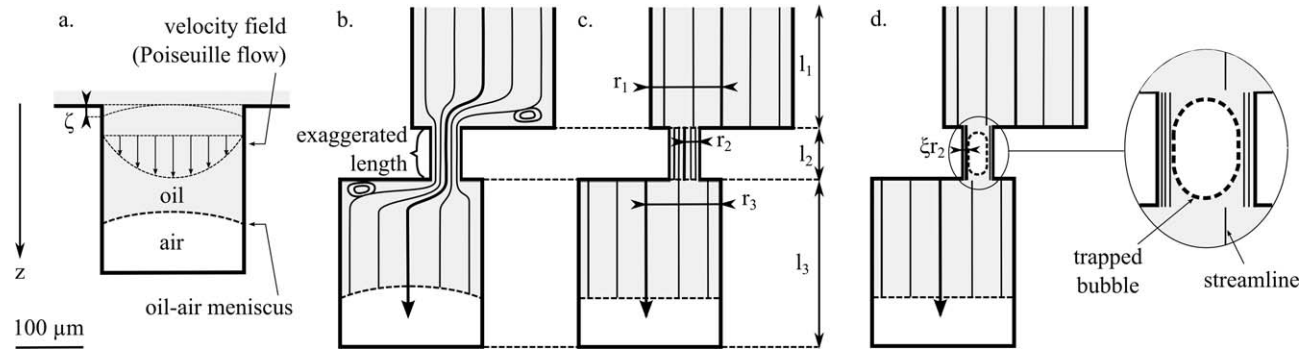

Figure 2. Capillary oil flow between two adjacent cells connected although a defect (the constriction length is exaggerated; see tissue details in Figure 1): (a) real oil meniscus shape and idealized Poiseuille velocity profile within a single cell, (b) real stream lines between connected cells, (c) idealized streamlines assuming Poiseuille flow, and (d) trapped bubble within the constriction.

In presence of variables sections, the continuity equation enforces that oil velocity in the upstream section $1 \le j < i$, denoted v_j, is related to the oil velocity front, dz/dt, in the ith section as $v_j = \frac{r_i^2}{r_j^2}\frac{dz}{dt}$, where r_i and r_j are the radii of section i and j, respectively. The integration by parts of Eq. 2 between $\zeta = 0$ (external surface) and $\zeta = z$ (oil front penetration in section i) combined with oil mass balance leads to

$$P_{(z)} - P_0 = -8\eta_{\text{oil}} \int_0^z \frac{v(\zeta)}{r_{(\zeta)}^2} d\zeta = -8\eta_{\text{oil}} \frac{dz}{dt}\left(\sum_{j=1}^{i-1}\frac{r_i^2}{r_j^4} l_j + \frac{r_i^2}{r_i^4}\left(z - \sum_{j=1}^{i-1} l_j\right)\right)$$
$$= -8\eta_{\text{oil}} \frac{dz}{dt}\left(\frac{z}{r_i^2} + \sum_{j=1}^{i-1} r_i^2\left(\frac{1}{r_j^4} - \frac{1}{r_i^4}\right) l_j\right) = -8\eta_{\text{oil}} \frac{dz}{dt}\left(\frac{z}{r_i^2} + \Delta_i^\eta\right) \tag{3}$$

where l_j is the length of the jth section, $\sum_{j=1}^{i-1} l_j \le z < \sum_{j=1}^{i} l_j$ and $\Delta_i^\eta = \sum_{j=1}^{i-1} r_i^2 (\frac{1}{r_j^4} - \frac{1}{r_i^4}) l_j$ is a correction factor, due to the variation of cross-sections, comparatively to an equivalent capillary tube of uniform radius r_i.

The average oil velocity and oil mass between positions 0 and z are given, respectively, as

$$v_i^{\text{oil}}(z) = \frac{1}{z}\frac{dz}{dt}\left(\sum_{j=1}^{i-1}\frac{r_i^2}{r_j^2} l_i + \left(z - \sum_{j=1}^{i-1} l_i\right)\right)$$
$$= \frac{1}{z}\frac{dz}{dt}\left(z + \sum_{j=1}^{i-1}\left(\frac{r_i^2}{r_j^2} - 1\right) l_i\right) = \frac{dz}{dt}\left(1 + \frac{\Delta_i^v}{z}\right) \tag{4}$$

and

$$\frac{m_i^{\text{oil}}}{\pi r_i^2} = \rho_{\text{oil}}\left(\sum_{j=1}^{i-1}\frac{r_j^2}{r_i^2} l_i + \left(z - \sum_{j=1}^{i-1} l_i\right)\right) = \rho_{\text{oil}}\left(z + \sum_{j=1}^{i-1}\left(\frac{r_j^2}{r_i^2} - 1\right) l_i\right)$$
$$= \rho_{\text{oil}}\left(z + \Delta_i^m\right) \tag{5}$$

The correction factors associated to oil velocity and mass conservation are $\Delta_i^v = \sum_{j=1}^{i-1}(\frac{r_j^2}{r_i^2} - 1)\frac{l_i}{z}$ and $\Delta_i^m = \sum_{j=1}^{i-1}(\frac{r_j^2}{r_i^2} - 1) l_i$, respectively. All three correction factors verify $\Delta_1^v = \Delta_1^m = \Delta_1^\eta = 0$.

By counting positive the displacements in the direction of gravity, the momentum balance of the oil volume located between positions 0 and z reads from Eqs. 4 and 5

$$\frac{d}{dt}\left(m_{\text{oil}}^i v_{\text{oil}}^i\right) = \rho_{\text{oil}}\left(\begin{array}{c} \dfrac{\left[z(t)+\zeta+\Delta_i^m\right]\left[z(t)+\zeta+\Delta_i^v\right]}{z(t)+\zeta}\dfrac{d^2 z(t)}{\partial t^2} \\ + \left(\dfrac{z(t)+\zeta+\Delta_i^m}{z(t)+\zeta} + \dfrac{z(t)+\zeta+\Delta_i^v}{z(t)+\zeta} - \dfrac{\left[z(t)+\zeta+\Delta_i^m\right]\left[z(t)+\zeta+\Delta_i^v\right]}{(z(t)+\zeta)^2}\right)\left(\dfrac{dz(t)}{dt}\right)^2 \end{array}\right) =$$
$$+ \frac{2}{r_i}\gamma(T)\cos\theta + \rho_{\text{oil}}(T) g \cos\beta\left[z(t)+\Delta_i^m\right] - 8\eta_{\text{oil}}(T)\frac{dz(t)}{dt}\left[\frac{z(t)}{r_i^2} + \Delta_i^\eta\right] + P_{\text{atm}} - P_{\text{air}}(t,T) \tag{6}$$

where T is the surface temperature, θ is the contact angle between the solid matrix, liquid and air, g is gravity, ρ_{oil} is the oil density and P_{atm} is the external pressure. As suggested in Refs. 56,76, ζ is as an infinitesimal liquid height—interpretable as the initial meniscus height—required to remove the singularity when Eq. 6 is integrated for the initial condition $z(t = 0) = 0$.

The main interest of Eq. 6 relies on its ability to describe the dynamics of oil penetration along a route with any arbitrary piecewise variation of cross-section areas. This variation can be either the consequence of a passage of oil through a small defect or due to the presence of captive air bubble. In the latter case, the parameters controlling the deviations to a uniform cross-section are a function of time: $\Delta_i^m(t)$, $\Delta_i^v(t)$, $\Delta_i^\eta(t)$. The equivalent description using the concept of permeability can be found in Ref. 75.

Air Escape Mechanims. In post-frying conditions, the parenchyma tissue forming the product crust is assumed to

be enough dry (no residual capillary water) so that oil can be considered as the wetting fluid and air as the non-wetting phase. Air composition can vary from pure superheated steam at the end of frying to surrounding air at the end of cooling. Air gas pressure,$P_{\mathrm{air}}(t,T)$, ahead the oil meniscus, facilitates or opposes to oil propagation depending on whether gas compression or steam condensation dominates. We call "spontaneous" imbibition and "forced" imbibition the situations corresponding to $P_{\mathrm{air}}(t,T)=P_{\mathrm{atm}}$ and $P_{\mathrm{air}}(t,T) < P_{\mathrm{atm}}$, respectively. Spontaneous imbibition restricted by air compression/release ahead the liquid front has been experimentally studied in Ref. 77. Oil–air counter-current flow configuration occurs when the wetting fluid (oil) is drawn into the pore space by capillary forces and when the non-wetting phase (air) is driven back through the wetting phase toward the opposite open end. This mechanism is very likely when the pores forming capillaries are open at only one face.

When capillaries are open at more than one end or when the capillary is polygonal, the spatial organization of phases becomes more intricate.[38,78] As a common rule, the wetting fluid will tend to fill more rapidly small cavities or throats and sharp corners, where the threshold capillary pressure is the highest.[79] Direct observations[80,81] and simulations[79,82] of spontaneous imbibition in networks with square channels showed that the wetting fluid at corners can displace in advance of the main front of the non-wetting one (e.g., air) before complete invasion of pore bodies. This mechanism referred to snap-off or chock-off contributes to expel air through defects created during frying at junctions between cells, and through thin holes distributed naturally all along cell walls. Only large trapped air bubbles can leave surface cells by buoyancy without snap-off, as experimentally observed in Ref. 20. In living parenchyma cells, cell-to-cell communication is mediated through specialized 50 nm thick plasma-lined tubular structures, so-called plasmodesmata.[83] In dried tissues, they are seen as pores or pits with either larger or smaller openings: about 20–100 nm.[84] Corner flow ceases either when the pressure difference $P_{\mathrm{atm}}-P_{\mathrm{air}}(t,T)$ increases or when capillary pressure at corners decreases sufficiently as a result of film thickening.[80] As an illustration, for channels with square cross-sections, wetting-liquid films detach from the interface at a critical capillary pressure given by[85]

$$p_{\mathrm{collapse}}=\gamma\frac{\cos\theta-\sin\theta}{r} \tag{7}$$

where r is the radius of the inscribed circumference.

Piston-type oil front displacements have conversely higher critical capillary pressure thresholds, $2\gamma\cos\theta/(rf)$ and are, therefore, favored in initially empty cells over snap-off. The involved factor $f \geq 1$ is a complicate function of the wetting history and on the number of neighboring throats already filled by the wetting fluid.[80,82] In fried products, undamaged or low-damaged cell walls are almost impermeable to oil in post-frying conditions (see figure 8 of Ref. 20) but exhibit a significant permeability to gases, either air or steam (e.g., steam flows typically through the thin crust against a pressure drop varying as low as few kPa, see Refs. 62,86). The exact contribution of random tissue defects (with variable size and geometry) and of the apoplastic pathways (i.e., through cell-walls) is unknown and complicates dramatically the achievable description of oil invasion. In our study, a simplified "phase averaged" oil flow description along the curvilinear coordinate z is adopted (see Eq. 6). The coexistence of oil and air at the same position z due to corner flows and snap-off effects is only considered via their corresponding air-escape mechanisms. In agreement with observations of Ref. 20, a counter-current (so called "counter") and two co-current oil–air flow configurations are hypothesized as sketched in Figure 3. Air counter-current flow is very likely only when air can cross constrictions as almost continuous slugs.[87] In co-current configurations, air escapes either by a defect at the bottom of the cell (so-called air "piston" flow) or through many thin pores/pits along cell walls (so called "transpiration" flow). The main difference between "piston" and "transpiration" air flow is that the number of "pores" available for air escape depends on the amount of oil filling the cell in the latter.

The variation of air pressure, P_{air}, depends on the isotherm compression of the air volume ahead the front and on the ability of air to escape. To keep the complexity tractable, we consider that the volume of air is trapped inside a tube of the same section as the meniscus and whose length is $z_{\mathrm{bottom}}-z(t)$, where z_{bottom} is the position of the end of the tube. By assuming that air can escape according to the three competing mechanism, the global air balance assuming possible isotherm air compression reads

$$\frac{dP_{air}(t)}{dt}=\frac{P_{air}(t)}{z_{bottom}-z(t)}\frac{dz(t)}{dt}-(P_{\mathrm{air}}(t)-P_{\mathrm{atm}})\times\left[\frac{\alpha_{\mathrm{piston}}}{z_{\mathrm{bottom}}-z(t)}+\frac{\alpha_{\mathrm{counter}}}{z(t)(z_{\mathrm{bottom}}-z(t))}+\alpha_{\mathrm{transpiration}}\right] \tag{8}$$

The corresponding effective transport coefficients $\{\alpha_k\}_{\substack{k=\mathrm{piston},\\ \mathrm{counter},\\ \mathrm{transpiration}}}$ are defined with more details in Ref. 18; they have units respectively in m s^{-1}, m^2 s^{-1}, and s^{-1}. The interpretation of each term within the square brackets as effective permeabilities is summarized hereafter. The resistance to air leak increases with the height of the oil column in counter-current oil–air flow, whereas the cross-section area participating to transpiration decreases with the reduction of the number of lateral "pores," which are not in contact with oil. Only the apparent permeability of the oil–air piston flow is independent of position. Equation 8 can be seen therefore as a generalization of the model of Ref. 55 to open systems. It is worth noticing that the capillary back pressure in the cell after snap-off (see Ref. 88) is not considered. In agreement with the direct observations of bubbles created by snap-off mechanism and their difficulty to rise by buoyancy in constrictions,[17,18,20] the variation of pressure due to air bubbles crossing the oil–air interface is also neglected. Conversely, the role of trapped bubbles in the reduction of oil passage is explicitly considered in the subsection "Delayed oil penetration between connected cells."

The system of ordinary differential Eqs. 6 and 8 integrated over time for proper initial conditions, $P_{\mathrm{air}}(t=0)$, $z(t=0)$, and $\frac{dz}{dt}|_{(t=0)}$, enables to simulate oil penetration along a tube with an arbitrary number of oil reduction passages (due to constrictions or trapped bubbles) and various oil–air flow mechanisms. The effects of steam condensation on oil uptake or the competition between air penetration and oil penetration on pressure recovery can be studied simultaneously.

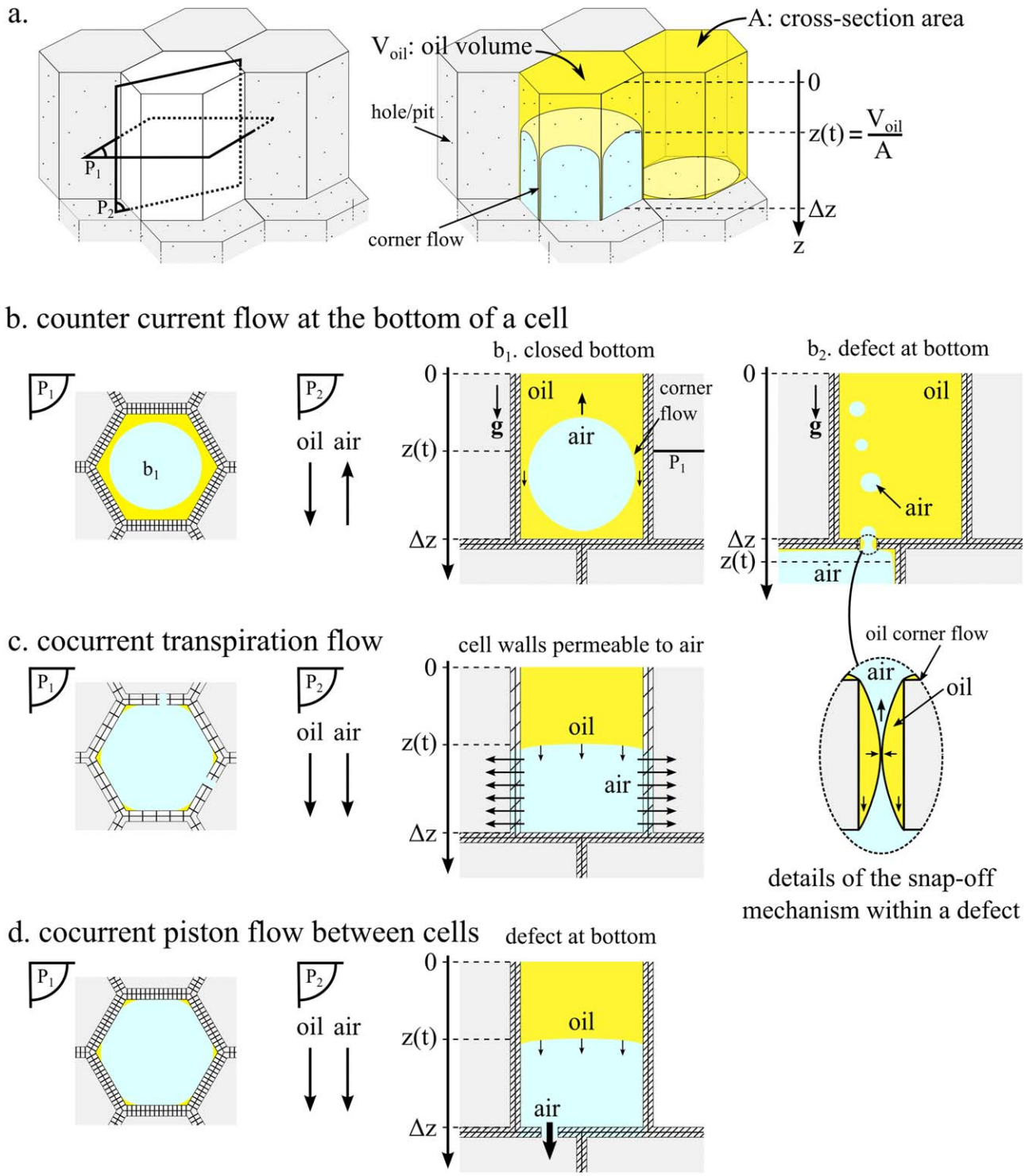

Figure 3. Oil–air displacements in the crust of a fried product (case of potato strip as shown in Figure 1; starch is not represented): (a) main and corner oil flows; (b–d) air escape mechanisms. $z/\Delta z$ represents the average volume filling ratio of the cell.

[Color figure can be viewed in the online issue, which is available at wileyonlinelibrary.com.]

Practical approximations of Eqs. 6 and 8 for individual cells

Approximate analytical solutions of Eqs. 6 and 8 can be derived when both equations are uncoupled. Practical approximations are presented to analyze the effective scaling of z with t, written as $z \propto t^s$, according to the considered air escape mechanism. Although the air transport as continuous phase (transparent phase) cannot be directly observed, the dominant escape mechanism can be indirectly identified by comparing the value of the scaling exponent, s, with the value identified from microscopic experiments of Ref. 20 (see also the Supporting Information).

Infinite Volume or Short Percolation Times. As discussed in general terms in Ref. 89, inertial flows cannot be

neglected when oil front passes thin capillaries or defects and when the pressure gauge is negative (steam condensation).[76,90] When $P_{atm}-P_{air}$ can be assumed constant and when the initial velocity of the oil entering into the capillary is negligible, Eq. 6, integrated between t_0 and t, gives[68]

$$z(t)^2=z(t_0)^2+\frac{2b}{a}\left((t-t_0)-\frac{1}{a}[1-\exp(-a(t-t_0))]\right) \quad (9)$$

with $a=\frac{8\eta_{oil}}{\rho_{oil}r^2}$ and $b=\frac{1}{\rho_{oil}}\left(P_{atm}-P_{air}+\frac{2\gamma\cos\theta}{r}\right)$.

For very short times ($t-t_0 \ll 1/a$), a three order serial expansion of Eq. 9 shows a linear dependence with time[91]: $z(t)^2-z(t_0)^2=bt^2$. When $t-t_0 \gg 1/a$, Eq. 9 is equivalent to the classical Lucas–Washburn equation.

Finite Volume Effects. In presence of a closed gas volume, capillary pressure, $p_C=\frac{2\gamma(T)\cos\theta}{r}$, is expected to be rapidly equilibrated with the internal overpressure, $P_{air}(t,T)-P_{atm}$, and the progression of oil front is stopped. When air can be released, oil progression follows continuously at almost constant pressure as experimentally shown.[77] Introducing $dP_{air}(t,T)/dt \approx 0$ for $t > t_0$ and neglecting inertia variation in Eqs. 6 and 8 leads to three analytical solutions corresponding to the three limiting air transport mechanisms

$$\begin{cases} z_{plug}(t)-z(t_0) \approx \min\left(\frac{\alpha_{piston}}{1+P_{atm}/p_C}(t-t_0), z_{bottom}-z(t_0)\right) \text{ with } \alpha_{counter}=\alpha_{transpiration}=0 \\ z_{counter}(t)^2-z(t_0)^2 \approx \max\left(\frac{2\alpha_{counter}}{1+p_{atm}/p_C}(t-t_0), {z_{bottom}}^2-z(t_0)^2\right) \text{ with } \alpha_{piston}=\alpha_{transpiration}=0 \\ \frac{z_{transpiration}(t)-z(t_0)}{z_{bottom}-z(t_0)} \approx 1-\exp\left(-\frac{\alpha_{transpiration}}{1+p_{atm}/p_C}(t-t_0)\right) \text{ with } \alpha_{piston}=\alpha_{counter}=0 \end{cases} \quad (10)$$

where $z(t_0)=z_{bottom}\left(1-\frac{P_{air}(t_0)}{P_{atm}+P_C}\right)$.

The performances of Eqs. 9 and 10 are presented in Figure 4 and compared to the full coupled model (6) and (8), which is solved numerically without the assumption of $dP/dt=0$. The conditions correspond to the penetration of oil within a single cell (350-μm length, cell radius of 100 μm) at 120°C with post-frying conditions detailed in Table 1. The values of $\{\alpha\}_{\substack{k=\text{piston,}\\ \text{counter,}\\ \text{transpiration}}}$ were chosen to slow down the oil displacement by two magnitude orders comparatively to a cell with infinite length. Spontaneous imbibition was associated to a capillary pressure, p_C, of 473 Pa as calculated from properties listed in Table 1 (see Figures 4a,c,e), whereas forced imbibition was simulated for the maximum negative pressure gauge of 40 kPa measured in Refs. 62,98 (Figures 4b,d,f). In our simulations, the ratio $z/\Delta z$ represents the volume filling of cells regardless the spatial arrangement of oil–air biphasic flows (see Figure 3) as described in Ref. 20 (see also Supporting Information).

The Lucas–Washburn equation (Eq. 9 with $a \to +\infty$) fits well the kinetics in cells of infinite length but with too low initial acceleration (Figure 4a). The discrepancy is even more significant when a negative pressure gauge (Figure 4b) is applied, as already noticed in Ref. 89. In finite systems, gas pressure increases during the first tenths of milliseconds while being almost aperiodic (Figure 4f) as discussed in Ref. 59. Spontaneous imbibition makes gas pressure oscillating with a pseudo period depending on the considered air escape mechanism (Figure 4e). Once the correct position of $z(t_0)$ is set, all proposed analytical solutions (10) fit remarkably the different behaviors.

Delayed oil penetration between connected cells

Change in diameters and biphasic oil–air flow delay dramatically the passage of oil from one cell to next one. Based on simple physical approximations, we show in this section that the associated filling and lag-times can be extrapolated by recurrence. As a result, large-scale simulations can be fed from observations of the filling kinetics of the very first cell layers.

Slowdown of Oil Flow in Successive Constrictions. Generalizing the previous reasoning to $N > 1$ cells (see Figure 2c for $N = 2$) with identical radii $r_1=r_3=\ldots=r_{2N-1}=r$ and separated by $N-1$ constrictions with identical radii $r_2=r_4=\ldots=r_{2N-2}=r_0$ and lengths $l_2=l_4=\ldots=l_{2N-2}=l_0$ leads to the following expression of the initial velocity at the beginning of each cell (see Eq. 4)

$$\left.\frac{dz}{dt}\right|_{\substack{\text{cell}\\ \text{begining}}}=\frac{r\gamma(T)\cos(\theta)}{4\eta_{oil}(T)}\frac{1}{z+r^2\Delta_N^\eta} \quad (11)$$

with $r^2\Delta_N^\eta=r^2\sum_{j=1}^{N-1}r^2\left(\frac{1}{r^4}-\frac{1}{r_0^4}\right)l_0=(N-1)l_0r^4\left(\frac{1}{r^4}-\frac{1}{r_0^4}\right)$ according to Eq. 3, which can be approximated by $(N-1)l_0\left(\frac{r}{r_0}\right)^4$ for r_0 sufficiently small comparatively to r. The effect of constrictions increases linearly with the number of crossed restrictions and as power low with the passage reduction. At the scale of few cells and for typical defects of few micrometers in cell walls, the reduction of the flow velocity is significant but decreases beyond one centimeter.

Interactions Between Oil and Air Flows. As experimentally shown in Ref. 20, oil percolates between connected cells at defects in cell walls and in cell junctions. If air is penetrating/leaving through the same pathways as oil if snap-off occurs, some bubbles may remain trapped and subsequently released. Bubble motions are expected to be governed by buoyancy forces in vertical channels and/or by back-pressure. The flow reduction consecutive to bubble obstruction in capillaries is broadly reported in the literature. The gas entrapment process in closed-end microchannels has been notably investigated in Refs. 99,100, giving the conditions of theoretical release at constrictions. The authors showed that the release process starts when the work of the pressure forces over the length of the trap exceeds the surface energy required for the trapped bubble to reenter within the constriction. By assuming a Poiseuille flow approximation, this condition on the work of the pressure can be replaced by a condition on the volume of displaced oil: the bubble is released when an enough amount of oil has flowed around the bubble. In the context of fried products, the presence of trapped bubbles in successive connected cells can occur randomly at different stages of oil penetration.

Oil penetration between two cells (see Figures 2c,d) connected through a constriction of 5 μm is described in

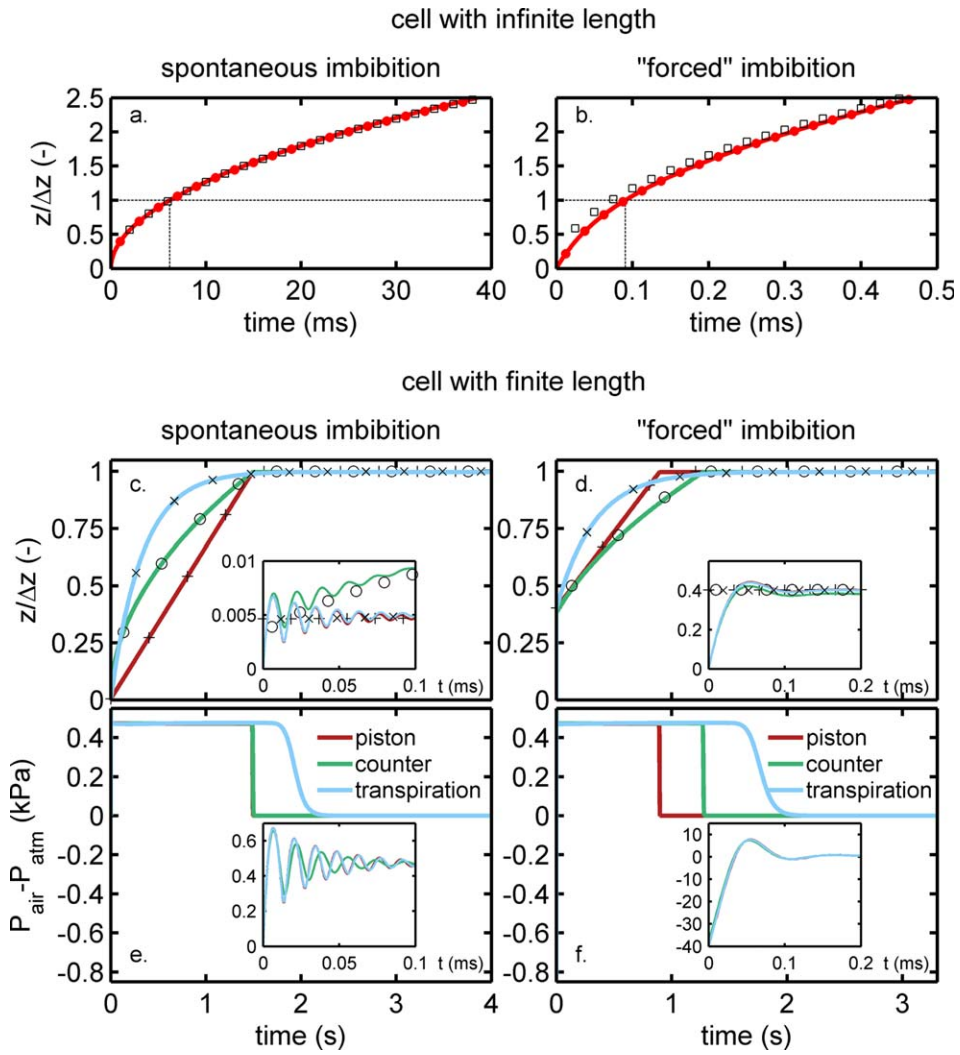

Figure 4. Oil–air front displacements in a circular-shaped cell with infinite (a-b) or finite length (c–f).

(a-b) Numerical solutions of Eq. 6 (continuous lines) are compared with analytical solutions (dots: Eq. 9; squares: Eq. 9 whith $a \to \infty$). (c–f) Numerical solutions of system (6) and (8) (continuous lines) are compared with analytical solutions of Eq. 10 (piston flow: symbol +; counter-current flow: circles; transpiration flow: crosses). Corresponding simulation conditions are listed in Table 1. Spontaneous and "forced" imbibition are associated respectively to $P_{atm} - P_{air}(t=0) = 0$ and $P_{atm} - P_{air}(t=0) = 40$ kPa (reproduces steam condensation effect). Air escape mechanisms are detailed in Figure 3. [Color figure can be viewed in the online issue, which is available at wileyonlinelibrary.com.]

Figure 5 without trapped air bubble (Figures 5a,b) and with air bubble obstructing 75% of the section (Figures 5c–e). The bubble was assumed to be released when 3% of the next cell has been filled. The corresponding effective radius accessible to oil flow with time is presented in Figure 5c. Other simulation parameters were similar to those used for simulations depicted in Figure 4 and reported in Table 1.

Without trapped bubble, both capillary pressure and meniscus velocity increase significantly in capillaries as thin as cell walls and drop dramatically when the meniscus enters in the next cell (Figures 5a,b). Pressure drop is followed by an abrupt change of the slope of z vs. t. Similar effects have been already reported in convergent-divergent configuration in Ref. 26,27. The reduction of the oil flow rate once the cross-section is traversed is governed by oil balance conservation (see Eq. 11).

Entrapped bubbles aggravate previous oil flow rate diminution by reducing additionally the effective hydraulic diameter by a coefficient $\xi(t) < 1$. The diminution can be so strong that the oil–air meniscus may seem to freeze at the entrance of the second cell (Figure 5d). Because trapping time was set reciprocally proportional to flow rate, the dwelling time of the meniscus at the beginning of the second cell increases as $(r/\xi(t)r_0)^4$, that is from 10^{-1} s to 2×10^2 s when r_0 was reduced from 100 μm down to 4 μm. Once the bubble is released, filling times of the second cell follow subsequently similar relationship but with $\xi(t)=1$. The exponent four combines both the increase of the drag and the acceleration within the constriction. Similar kinetics as those reported in Figure 5d can be found in Figures 4 and 5 of Ref. 100.

Practical Approximations. In the remaining part of the work, the following simplifications will be considered to simulate oil uptake at the scale of many connected cells in presence of an air/gas or not.

1. The trapping and release process of air bubbles is replaced by an equivalent delay (Δt_{lag}) between the successive filling kinetics of connected cells, with bottom positions denoted $z_{i,bottom}$ and $z_{i+1,bottom}$, respectively

Table 1. Parameters of the Micromodel Used in This Study: Additional Geometry Details Are Presented in Figures 2 and 3

Property			Meaning	Value	Figure	Ref.
Post-frying conditions		T	Temperature	120°C	4–5	90
		P_{atm}	Atmospheric pressure	10^5 Pa	4–5	–
		P_{air}	Spontaneous imbibition "forced" imbibition	10^5 Pa6 × 10^4 Pa	4–5	90
Geometry		r	Apparent cell radius	100 μm	4–5	20
		Δz	cell height	350 μm	4–5	92,93
		r_0	Apparent constriction radius	4–100 μm	5	Variable
		ξ	Fraction of r_0 kept free when a air bubble is trapped within the constriction	0.25	5	This work
		l_0	Constriction height (commensurable to wall thickness)	3 μm	5	94,95
Oil properties		γ	Oil surface tension at 120°C	0.03 N m^{-1}	4–5	16
		θ	Contact angle between oil, air and restructured potato product	0.663 rad	4–5	96
		ρ_{oil}	Density of oil at 120°C	865 kg m^{-3}	4–5	97
		η_{oil}	Dynamic viscosity of oil at 120°C	0.06 Pa s	4–5	97
Air escape property	Layer 1	$\alpha_{piston,1}$*	Effective transport coefficient of air under piston flow mechanism (see Eq. 10)	5.0×10^{-2} m s^{-1}	4	20
		$\alpha_{counter,1}$*	Effective transport coefficient of air under counter-current flow mechanism (see Eq. 10)	8.7×10^{-6} m^2 s^{-1}	4–5	20
		$\alpha_{transpiration,1}$*	Effective transport coefficient of air under transpiration mechanism (see Eq. 10)	650 s^{-1}	4	20
	Layer 2	$\alpha_{transpiration,2}$†	Effective transport coefficient of air under transpiration mechanism (see Eq. 10)	98 s^{-1}	5	20

Rate constants $\{\alpha_{k,i}\}_{k=\text{piston, counter, transpiration}}$ from Ref. 20 correspond to filling times of *1.5 s in Layer 1 and †a minimum of 10 s in Layer 2.

$$z(t)=z_{i,\text{bottom}} \text{ while } t_{i,0}+\Delta t_{i,\text{fill}} \le t \le t_{i,0}+\Delta t_{i,\text{fill}}+\Delta t_{i,\text{lag}}=t_{i+1,0} \tag{12}$$

with $\Delta t_{i,\text{fill}}$ the time required to fill one cell of layer i starting at time $t_{i,0}$.

2. The filling kinetic of an individual cell obeys to a truncated first-order kinetic

$$\frac{z(t)-z(t_{i,0})}{z_{i,\text{bottom}}-z(t_{i,0})}=\min\left[\frac{1}{\varsigma}\left(1-\exp\left(\frac{t-t_{i,0}}{\Delta t_{i,\text{fill}}}\ln(1-\varsigma)\right)\right),1\right] \tag{13}$$

controlled by a shape factor $0<\varsigma<1$ ($\varsigma\to 0$ and $\varsigma\to 1$ giving a linear and an exponential model, respectively). $\Delta t_{i,\text{lag}}+\Delta t_{i,\text{filling}}$ is the effective time required to fill the cell of layer $i \ge 2$.

The main advantage of Eqs. 12 and 13 is that they reproduce the exact filling kinetics of connected cells parameterized by $\Delta t_{1,\text{fill}}, \Delta t_{1,\text{lag}}, \Delta t_{2,\text{fill}}, \Delta t_{2,\text{lag}}, \ldots$, whenever the exact mechanism inside each cell tends to deviate from microscopic Eqs. 6 and 8. As a result, micromodel Eqs. 12 and 13 can been seen as a coarse-grained version of (6) and (8). Because the size and type of defects are highly variable, $\{\Delta t_{i,\text{fill}}\}_{i\ge 2}$ and $\{\Delta t_{i,\text{lag}}\}_{i\ge 2}$ values are expected to be broadly distributed and increasing from one cell to the next one as shown in Ref. 20.

In absence of air, $\{\Delta t_{i,\text{lag}}\}_{i=1..N}=0$ and $\{\Delta t_{i,\text{fill}}\}_{i=2..N}$ decrease linearly with the number N of constrictions as predicted by Eq. 11. Hence, the time to reach the ith cell below the surface with $i>1$ and separated by $i-1$ similar constrictions is

$$\Delta t_{i,\text{fill}}=-\frac{\ln(1-\varsigma)}{\varsigma}\Delta z\left(\frac{dz}{dt}\Big|_{t\to t_0}\right)^{-1} \approx -\frac{\ln(1-\varsigma)}{\varsigma}\frac{4\eta_{oil}(T)}{r\gamma(T)\cos(\theta)}\left(z+(i-1)l_0\left(\frac{r}{r_0}\right)^4\right)\Delta z \tag{14}$$

where Δz is the typical cell length. The filling time increment between consecutive cells is

$$\Delta t_{i+1,\text{fill}}=\Delta t_{i,\text{fill}}-\frac{\ln(1-\varsigma)}{2\varsigma D_o(T)}\left(\Delta z+l_0\left(\frac{r}{r_0}\right)^4\right)\Delta z \tag{15}$$

For small r values, Eq. 15 deviates significantly from advection: $\Delta t_{i+1,\text{fill}}=\Delta t_{i,\text{fill}}$. This behavior is the consequence of the mass conservation: to fill the ith+1 cell, the ith cell requires to be continuously filled while considering a

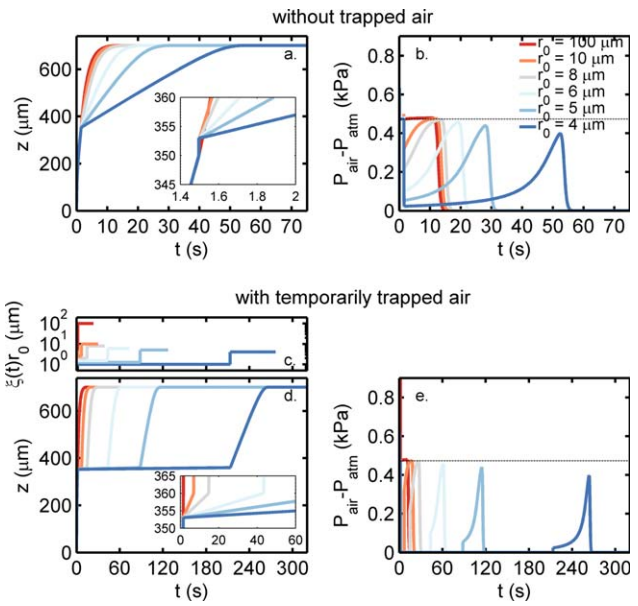

Figure 5. Oil–air front displacements between two circular-shaped cells ($r = 100$ μm; $\Delta z = 350$ μm) connected by a defect of radius r_0 without (a-b: $\xi(t) = 1$) and with (c–e: $\xi(t) \le 1$) trapped bubble.

The corresponding situations are depicted in Figures 2c, d, respectively. The trapped bubble is assumed to cause a passage reduction of $\xi = 0.75$ and to be released when 3% of the next cell is filled with oil. [Color figure can be viewed in the online issue, which is available at wileyonlinelibrary.com.]

stationary flow. The ratio $D_o(T)=\frac{r\gamma(T)\cos(\theta)}{8\eta_{oil}(T)}$ is hence consistent with a one-dimensional (1-D) diffusion coefficient with a value of about 4.9×10^{-6} m^2 s^{-1} for $r=100$ μm at 120°C (see Table 1). By considering $\Delta z=350$ μm and oil crossing small defects of length $l_0=3$ μm and radius $r_0=10$ μm, an increment of about 2.36 s (for $\varsigma=0.9$) is found between connected cells. That is to say, the time to fill the cells of the fourth layer (after crossing three constrictions of 10 μm) is expected to last 7.08 s longer than for the filling of the first layer. In real frying conditions, this time can be much longer as oil viscosity increases rapidly with decreasing temperature. Drag effects increase delays 39 times when r_0 is reduced from 10 μm down to 4 μm. It is consequently thought that oil could not permeate through defects smaller than 1 μm. This interpretation would corroborate the extremely low permeability of cell walls to oil.[20] It is worth noticing that ς is a phenomenological parameter derived from the coarse graining procedure. It could be interpreted as the partial filling ratio triggering oil flow from one cell to the next one.

Snap-off mechanism can trap a bubble in defects while enabling oil to flow around the bubble. In this study, the events which create the bubble are assumed to occur at random, but their consequence on oil flow reduction is explicitly considered. In details, experimental works in nonaxisymmetric capillaries[101,102] showed that the mechanism of bubble snap-off was rate dependent and that the residual oil flow was associated to the retreat of oil meniscus at corners. By assuming that the bubble is released after the oil front displaces over a distance $\upsilon\Delta z$ (with υ a small positive number, see section "Interactions between oil and air flows" for justifications), Eq. 13 can be generalized to include the lag-time associated to a temporary oil passage reduction of r from r_0 down to ξr_0 with $0<\xi<1$

$$\begin{aligned}\Delta t_{i+1,\text{fill}}^{\text{with bubble}}&=\Delta t_{i+1,\text{lag}}-\frac{\ln(1-\varsigma)}{2\varsigma D_o}\left((1-\upsilon)\Delta z+l_0\left(\frac{r}{r_0}\right)^4\right)\Delta z \text{ with } \upsilon>0\\&=\Delta t_{i,\text{fill}}^{\text{with bubble}}-\frac{\ln(1-\varsigma)}{2\varsigma D_o}\left(\upsilon\Delta z+l_0\left(\frac{r}{\xi r_0}\right)^4\right)\\&\quad\Delta z-\frac{\ln(1-\varsigma)}{2\varsigma D_o}\left((1-\upsilon)\Delta z+l_0\left(\frac{r}{r_0}\right)^4\right)\Delta z\\&=\Delta t_{i,\text{fill}}^{\text{with bubble}}-\frac{\ln(1-\varsigma)}{2\varsigma D_o}\left(\Delta z+l_0\left(\frac{r}{r_0}\right)^4\left(1+\frac{1}{\xi^4}\right)\right)\Delta z\end{aligned} \tag{16}$$

Equations 15 and 16 show that lag-times and filling times without bubbles are closely related for sufficient small ξ and υ values as $\Delta t_{i+1,\text{lag}}\approx\frac{1}{\xi^4}\Delta t_{i+1,\text{fill}}$.

Materials and Methods

Dynamic imaging of oil uptake at microscopic scale

Three-dimensional oil percolation kinetics in potato parenchyma tissues were reconstructed from observations described in Ref. 20. Oil at 120°C was available in excess and located on top of two layers-thick emptied cells (i.e., with starch and cell content removed) maintained at 100°C. Cells were initially filled with air at atmospheric pressure and spontaneous imbibition of dyed oil was monitored dynamically on an inverted microscope in epi-fluorescence configuration using a 290 nm synchrotron source. The cells of the second cell layer adhered strongly to the coverslip so that the bottom of the second layer could be considered as closed. Raw images used in this study consisted in sequences comprising from 300 up to 1500 frames (1024×1024 pixels^2 with a lateral resolution 1.24 μm) acquired at a rate of one frame/s. Within each image, fluorescence was split into two channels corresponding to cell walls and oil signals, respectively. Cell contours were finally digitalized in 3-D from both 2-D projected images and 3-D image stacks.

Reconstruction of the oil–air front $z^{(t)}$ from observations

Previous treatments detailed in Ref. 20 considered only projected images. This study provides an interpretation along the direction z (oriented downward) based on an optical model detailed in the Supporting Information. Using the separation of time scales between the filling kinetics of successive cell layers, the following first-order approximation was used to infer the position of the oil–air front, $z^{(t)}$, from cell-averaged fluorescence intensities, $I^{(t)}$

$$\frac{I^{(t)}-I^{\left(t+\Delta t_{i,\text{lag}}\right)}}{I^{(t)}-I^{(t_i)}}\approx\frac{z^{(t)}-z_1}{z_i-z_{i-1}}+\text{o}\left(\frac{\left(z^{(t)}-z_{i-1}\right)^2}{\left(z_i-z_{i-1}\right)^2}\right)\quad\text{with}\begin{cases}t_{i-1}+\Delta t_{i,\text{lag}}\le t\le t_i\\ z_{i-1}\le z^{(t)}\le z_i\end{cases} \tag{17}$$

where $\{t_i\}_{i=0,1,2}$ is the time when the front reaches the separations between cells at position $\{z_i\}_{i=1..2}$. $\left\{\Delta t_{i,\text{lag}}\right\}_{i=1,2}$ is the apparent delay before the cell of the ith cell layer starts to be filled due to the delayed release of trapped bubbles, with $\Delta t_{1,\text{lag}}=0$ in tested conditions. As one cell was placed on top of three cells beneath (Figure 1d of Supporting Information), it is worth noticing that $I^{(t)}$ was averaged over different cell contours when the next cell was filled. Air bubbles rising in the opposite directions of oil, clearly visible in some frames, caused temporal fluctuations of $I^{(t)}$ (see eq. 1 in Supporting Information).

Identification of filling and lag-times from experimental $z^{(t)}$ kinetics

The effective imbibition model set by Eqs. 12 and 13 was fitted to all percolation pathways identified in the series of experiments with $\varsigma=0.95$. The three free parameters were the times required to fill each cell and $\Delta t_{2,\text{lag}}$. Continuous distributions were consistently achieved by assuming that they were Gamma distributed

$$pr(x=t)=\frac{1}{b_\Gamma^{a_\Gamma}\Gamma^{(a_\Gamma)}}t^{a_\Gamma-1}e^{\frac{t}{b_\Gamma}} \tag{18}$$

where $\Gamma^{(x)}$ is the Gamma function and x is a shorthand for any of the random variables: $\Delta t_{1,\text{fill}}$, $\Delta t_{2,\text{fill}}$, $\Delta t_{2,\text{lag}}$. The method of Ref. 103 was used to estimate the shape and scale parameters, a_Γ and b_Γ respectively, as well as their confidence intervals.

In this study, Gamma distributions are envisioned as a generalization of exponential ones and justified as follows. The process of trapping and release of air bubbles is assumed to be Poissonian so that lag-times are Erlang or Gamma distributed. For filling times, the justification is less intuitive. According to Eq. 15, choosing a log-normal conjugate prior distribution for the size of the defect, r_0, leads to a conjugate posterior distribution for the increment $\left\{\Delta t_{i+1,\text{fill}}-\Delta t_{i,\text{fill}}\right\}_{i\ge1}$, which is also a log-normal one. In practice, log-normal and Gamma distributions are closely related with similar tails while presenting significant

differences only for low values. Finally, without a loss of generality, it is important to notice that the use of Gamma distributed increments facilitates their extrapolations in simulation scenarios involving more than two layers as the sum of independent increments follows in this case also a Gamma distribution.

Simulation of oil uptake at the scale of a whole parenchyma tissue

A general and flexible framework has been designed to simulate oil uptake with arbitrary cell arrangements (i.e., based on 3-D real digitized structures) and underlying physics (with or without air, with constant pressure or not).

Common Assumptions. This article reports the principles in a simple case: (1) all cells have similar geometry and are arranged within a regular honeycomb structure, (2) the cut surface is parallel to the minimal cross-section of cells (assumption very realistic for potato chips and acceptable for French-fries), (3) oil percolates only through faces parallel to the surface, (4) oil is assumed to be available in an unlimited amount and to cover uniformly the external surface, (5) oil–air front displacement inside each individual cell along the cell longitudinal direction is described at coarse-grained level as detailed in section "Theory," (6) temperature is constant as in experiments of Ref. 20, (7) cell walls (and possibly starch) are at glassy state or near their glassy transition temperature and do not swell in contact with oil. The principles of homogenization in time and space remain similar in more complex configurations. The condition of an unlimited amount of oil at the beginning of frying may appear excessive at first sight but it corresponds to the observations of Ref. 17, who showed that cooling the product onto a thick film of oil was not affecting the final oil concentration profile in French-fries. Oil uptake is indeed a very fast superficial phenomenon occurring within the first second of cooling for the first cell layer and whose penetration depth is mainly limited by the presence of defects.[20]

Two aspects of the "random nature" of the real oil uptake mechanism are explicitly considered: (1) damage occurrence and types are randomly distributed in fried products (see discussion in Ref. 18 for French-fry type products), (2) air bubble trapping/release mechanism associated to highly heterogeneous first-passage times. Both contributions are, however, treated differently. Randomness in space is managed by generating randomly several and sufficiently large and periodic 3-D tissues according to prescribed rules. A tag "damaged" or "not damaged" is assigned to each cell according to distributions mimicking the real frying process of food products (e.g., potato strips or chips). As an illustration, the cells of the first cell layer are cut during the industrial process. If their content is fully removed, they are all considered as damaged. They may be considered partly "healed" (i.e., undamaged) if some starch fills partly the cells. Oil can percolate from one cell to the next one only if both adjacent cells are damaged. Because no oil is initially present, only damaged cells connected with the external surface by at least one continuous chain of damaged cells can be filled with oil.

At this stage, damaged or "fillable" cells are identified but the sizes of defects and the amounts of trapped air are still unknown. This information is introduced subsequently by assigning at random specific conductances between cells (equivalently filling and lag-times) according to *a priori* distributions. When it is combined in Eq. 13, it leads to a coarse description of oil percolation at cell level. Only the displacement along the longitudinal direction is preserved and the details of biphasic arrangement of oil–air phases are lost. This separation of times scales to reach one "fillable" cell and to fill the considered cell is in good agreement with both theory (see Eqs. 15 and 16) and experiments.[20] To reach a fast convergence while integrating the possibilities to have several routes to reach a same "fillable" cell, a Kinetic Monte-Carlo (KMC) methodology was applied with an algorithm of first-passage (see Ref. 104 and its relationship with KMC treatment in Ref. 105). The methodology is thought in particular to mimick well the randomness of the trapping-release process of air bubbles limiting the passage of oil and being responsible for the increase of oil residence time in cells.

Model 3-D Structure and Implemented Percolation Rules. The potato parenchyma structure was idealized as a 3-D solid foam organized in a perfect honeycomb-like prismatic structure.[106] Each cell was built from the extrusion of a regular hexagon. Starting from a cell placed at the center of the domain, a hexagonal tiling was subsequently obtained by joining three additional hexagons at each free vertex. Along the z direction, the successive N layers were shifted to reach a periodic structure over a period of two cells so that the position on the plane (x,y) of the common junction of three adjacent cells matched the position at the center of the cell immediately above and below. Cell walls were defined as the volume outside the effective internal volume. In the plane (x,y), the circular arrangement of cells led to a hexagonal tile shape with a rotational symmetry of order 6. To simulate an infinite surface with no edge, hexagonal periodic boundary conditions were applied as reproduced in Figure 6. The six hexagonal blocks (including 381 cells each) are fictive images of the central block and illustrate the connectivity of opposite cells due to the applied periodic boundary conditions.

Oil was assumed to percolate only in the z direction according to the adjacency matrix $\mathbf{A}_i=\left(a_{k,l}\right)_i$ giving the connectivity of the kth cell in layer i with the lth cell in layer $i+1$. The condition $\mathbf{A}_0=\mathbf{I}$ enforced that all cells of the top surface were accessible to oil after cutting. The adjacency was built to integrate boundary conditions in the plane (x,y), with the result that any cell (except those from the last layer) was located on top of three cells. Oil could migrate between layers but could not be transferred laterally within the same layer, as experimentally observed.[20] It is worth noticing that the overlap of cells in z direction enabled however oil to spread in the plane (x,y) when oil progressed along direction z. The maximum spread was limited only by the number of layers N and cell damage ratios.

For production, the tissue was simulated as a honeycomb arrangement of $N = 3$ to 12 layers and with a tiling radius of 100 cells (30,301 cells/layer). Hexagonal cell units had a depth of 350 μm and a surface area corresponding to an equivalent diameter of 200 μm. To enable a comparison with a real product, the proposed model tissue is equivalent in size to one quarter of the surface area of a French-fry of $100 \times 9 \times 9$ mm^3. Results were repeated ten times on structures with different random damages to get reliable statistics and properly homogenized estimates.

Dynamic Simulation of Oil Penetration Front. Possible oil percolation routes on N_S periodic parenchyma structures including N layers were sampled using a Kinetic Monte-

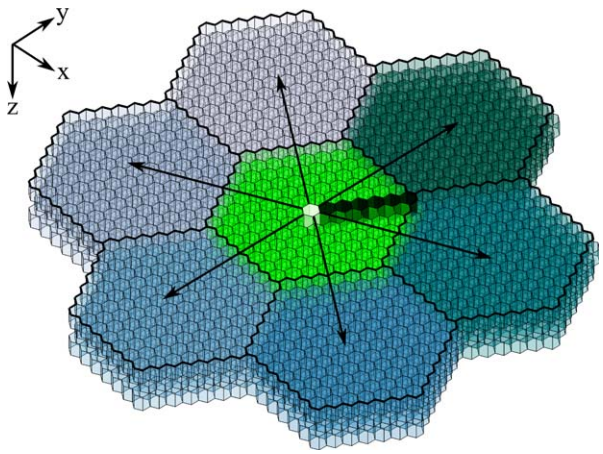

Figure 6. $N = 3$ layers crust details (see Figure 1) with its six fictive images (periodic boundary conditions).

The central hexagonal tissue (in green) of radius 6 cells comprises a total of 381 cells. Along the vertical direction, the structure is of period two (i.e., cells of adjacent layers are overlapping). The presented system is 30 times smaller than those used for production. [Color figure can be viewed in the online issue, which is available at wileyonlinelibrary.com.]

Carlo (KMC) sampling based on N_{MC} trials per structure (chosen as a number larger than 10^4/damage ratio of the first layer). By contrast with concurrent techniques such as finite element or finite volume methods, KMC methodologies enable to treat time continuously without limitation on the range of time scales. They have been developed in physical chemistry to simulate phenomena occurring on a broad range of frequencies. Applications to mass transfer can be found in Ref. 60,107. Basically, the KMC method explores stochastically a sequence of transitions (oil passage from one cell to the next one) between different states of the model, by choosing the links and events according to their probabilities of occurrence and/or the rates of the transitions.

In our case, the rates of the transitions (reciprocal times) are determined by the filling times and possible lag-times, whose first moment is given by the micromodel (see Eqs. 15 and 16). Their full distributions are given by Eq. 18. Without optimization and starting from a collection of filled cells, the naïve algorithm would consist in picking randomly filling and lag-times for all possible transitions according to prescribed distributions. The transition with the shortest total time should be selected, the corresponding continuous front displacement of oil–air should be simulated/reconstructed with the micromodel and the simulation clock should be incremented of the same amount. The list of transitions should be updated and the whole procedure should be repeated. This implementation suffers, however, several drawbacks: (1) the distributions of filling times do not take into account the effects of branching and (2) the sampling procedure does not consider the separability of filling events for cells belonging to the same layer.

The originally nonbranched micromodel (see Eq. 15) was extended to branched routes by replacing, for each cell i in a set, $\Delta t_{i-1,\mathrm{fill}}$ by the corresponding first-passage time, denoted $T_{i,FP}$. The importance of passage/arrival time distributions stems from the mechanism of cell filling itself: the cell is filled by the first meniscus, which is capable to reach it. By assuming that $N_{i,P}$ routes (possibly overlapping) connect the external surface to the targeted ith cell and by noticing that surface cells are independent entry points, the average time to reach the cell i is given by

$$T_{i,FP} = \Delta t_{i,\mathrm{lag}} + \frac{1}{\sum_{u=1..N_{i,P}} \frac{1}{T_{i,u}}} \tag{19}$$

where $\{T_{i,u}\}_{u=1..N_P}$ are average residence times within each branch.

Equation 19 is similar to Eq. 13 in Ref. 60 The scaling of first-passage times in self-similar structures with arbitrary branching is specifically discussed in Ref. 108. As all branches have the same length (connections occur only between cell layers in the current version), residence times tend to be homogeneous in time and the diffusive behavior is globally preserved in the branched generalization of the micromodel. In practice, all percolation paths were identified from the non-zero terms of $\prod_{i=0}^{N} \mathbf{A}_i$. Values of $\{T_{i,u}\}_{u=1..N_P}$ were calculated by recurrence by maintaining a table of first-passage times for all cells connected to the outside. Branched sampling was finally reduced to non-branched simulation by choosing randomly pathways with weights proportional to their reciprocal residence times. Oil front displacements were sampled and recorded optimally along a prescribed list of connected cells. For each cell in the set, one route to fill it was picked based on an exhaustive catalogue of all possible pathways including the cells in the set or not (i.e., neighboring cells). As a result, cells in the set could be filled, as expected in a real tissue, in a

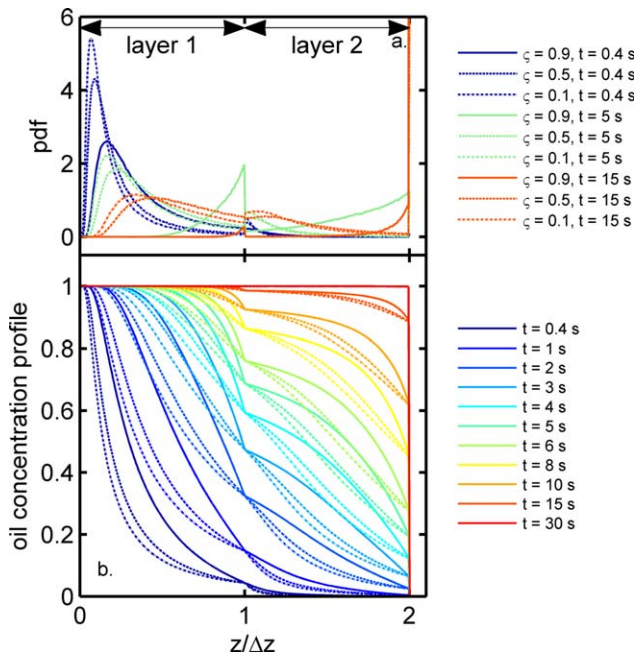

Figure 7. Principles of time homogenization of oil–air displacements between two connected cells of length Δz: Distributions of positions (a) for the three typical values of ς (solid line: 0.9, dashed line: 0.5, dotted line: 0.1); corresponding saturation profiles (b) calculated via Eq. 2021.

[Color figure can be viewed in the online issue, which is available at wileyonlinelibrary.com.]

nonsequential way: for example, the cell of the third cell layer might be filled before the cells above because a preferential route exists to reach it. The whole algorithm is outlined as follows

```
build the adjency matrix of the parenchyma structure
for j=1..N_S
  assign average filling times and lag-times
  build all percolation paths starting from the surface
  tabulate average first-passage times by recurrence
  for k=1..N_MC
    pick at random one percolation route : P_L with L any of 0..N
      for i=1..L
        enumerate all paths to reach the ith cell of P_L
        pick randomly one path based on their first-passage time distribution
        pick randomly filling and lag time values according to their distributions
        calculate the continuous displacements of the oil-air front in the ith cell
        store a discretized version in time of z(t)
```
(20)

Continuous oil front displacements $z(t)$ were calculated with Eq. 13 with a shape factor ς of 0.95, in agreement with model experiments of Ref. 20. When oil uptake was simulated without air initially filling cells, a profile without asymptotic behavior (see Eqs. 9 and 10) was preferred by choosing $\varsigma=0.5$.

Spatial and Temporal Homogenization. Continuous saturation profiles $s(z,t)$ were finally calculated from the cumulated distribution of the oil front position at some prescribed times t

$$s^{(z,t)}=\left\langle s_{j,k}^{(z,t)}\right\rangle_{\substack{\text{all paths } j=1..N_{\text{MC}} \\ \text{all structures } k=1..N_S}} =pr\left(z_{KMC}^{(t)}\big|_{\{\Delta t_{i,\text{lag}},\Delta t_{i,\text{fill}}\}_{i=1..N}}\geq z\right)=1-pr\left(z_{\text{KMC}}^{(t)}\big|_{\{\Delta t_{i,\text{lag}},\Delta t_{i,\text{fill}}\}_{i=1..N}}<z\right) \tag{21}$$

where $z_{\text{KMC}}^{(t)}$ is the oil front position sampled with the KMC algorithm (21).

Equation 21 provided a mean-field approximation of oil imbibition microscopic details, whereas details of the dynamics were captured by filling rates, lag-times, and cell connectivity. As a result, simulations based on complex oil–air flows through variable defects between cells could be ruled without strong assumptions on real transport properties. The principles of temporal homogenization are illustrated in Figure 7 on a simple configuration involving $N=2$ layers by assuming (1) that all cells of the second cell layer are connected with the cells of the first layer and (2) that filling kinetics obey to $\Delta t_{1,\text{fill}}\sim\Gamma(1.5,2.5)$ and $\Delta t_{2,\text{fill}}\sim\Gamma(1.5,2.5)$, with $\Delta t_{1,\text{lag}}=\Delta t_{2,\text{lag}}=0$. The results are plotted for three typical values of ς. It is worth noticing that the change in slope of the saturation profiles at the junction between cells is all the higher than the oil front displacement is more nonlinear with time (i.e., when $\varsigma\rightarrow 1$).

For real tissues, the distributions of $\left\{\Delta t_{i,\text{fill}},\Delta t_{i,\text{lag}}\right\}_{i=1..N}$ are likely to be unknown; but they can be estimated from Eqs. 15 and 16 using either (1) a proper Monte-Carlo sampling procedure with *a priori* distributions of defect radii and bubble obstructions, or (2) from mathematical properties of Gamma distributions. In this work, the latter was preferred by noticing that the sum of n independent Gamma random variables $\left\{X_i\sim\Gamma_{(a_i,b_i)}\right\}_{i=1..n}$ is a random variable following also a Gamma distribution $\Gamma_{(a_S,b_S)}$. The Welch–Satterthwaite approximation leads to $a_S=\left(\sum_{i=1..n}a_ib_i\right)^2/\sum_{i=1..n}a_ib_i^2$ and $b_S=\sum_{i=1..n}a_ib_i^2/\sum_{i=1..n}a_ib_i$, that is to say, $a_S=na_1$ and $b_S=b_1$ when all defects obey to similar distributions. As a_S is the shape factor of the resulting distribution, the approximation describes consistently the broadening of filling times with the number $n-1$ of crossed constrictions. For a tissue including homogeneous defects, the scaling

parameter b_S remains constant for all layers and depends only on the distribution of the size of defects, r_0, used by oil to cross from one layer to the next one. By noticing that the expectation of the resulting distribution is $a_S b_S$, observations from few layers (e.g., a_1 and b_1 values) can be generalized to more layers via a probabilistic version of Eqs. 15 and 16. By denoting $\{\Delta t_{i,\mathrm{fill}} \sim \Gamma(a_\Gamma^{i,\mathrm{fill}}, b_\Gamma^{i,\mathrm{fill}})\}_{i=2..N}$ and $\{\Delta t_{i,\mathrm{lag}} \sim \Gamma(a_\Gamma^{i,\mathrm{lag}}, b_\Gamma^{i,\mathrm{lag}})\}_{i=2..N}$, one gets

$$\begin{cases} a_\Gamma^{i+1,\mathrm{fill}} = a_\Gamma^{i,\mathrm{fill}} + \dfrac{\langle \Delta t_{i+1,\mathrm{fill}} \rangle - \langle \Delta t_{i,\mathrm{fill}} \rangle}{b_\Gamma^{i,\mathrm{fill}}} \\ a_\Gamma^{i+1,\mathrm{lag}} = a_\Gamma^{i,\mathrm{lag}} + \dfrac{\langle \Delta t_{i+1,\mathrm{lag}} \rangle - \langle \Delta t_{i,\mathrm{lag}} \rangle}{b_\Gamma^{i,\mathrm{lag}}} \end{cases} \quad \text{for } 1 \le i < N \qquad (22)$$

where $\{\langle \Delta t_{i,\mathrm{fill}} \rangle\}_{i=2..N}$ and $\{\langle \Delta t_{i,\mathrm{lag}} \rangle\}_{i=2..N}$ are the expectations of $\{\Delta t_{i,\mathrm{fill}}\}_{i=2..N}$ and $\{\Delta t_{i,\mathrm{lag}}\}_{i=2..N}$ as given respectively by Eqs. 15 and 16. Although recursion rules were inferred from nonbranched percolation routes, they were also applied to set *a priori* probabilities in real parenchyma structures.

To enable comparison with experimental results, oil uptake was finally calculated respectively to the solid basis from the local oil saturation, $s^{(z,t)}$, as

$$F_S^{(z,t)} = \frac{\varepsilon \rho_{\mathrm{oil}}^{(T)}}{(1-\varepsilon)\rho_s} s^{(z,t)} \qquad (23)$$

where, ρ_s and $\rho_{\mathrm{oil}}^{(T)}$ are the densities of solid and oil (i.e., cell walls) and ε is the average porosity of the parenchyma structure.

Results and discussion

Experimental determination of simulation parameters

Main input parameters, including geometry of cells and conduction rates from one layer to the next one, were inferred from static and dynamic observations collected by Ref. 20 on emptied parenchyma cells (no starch) initially filled with air. As dynamic observations were acquired exclusively in the plane (x,y), the displacements of the position of the oil front along direction z were reconstructed from the simplified optical model detailed in Supporting Information and with practical relationship, (17). Corresponding cell filling kinetics of individual cells were abstracted as $\{\Delta t_{i,\mathrm{lag}}, \Delta t_{i,\mathrm{fill}}\}_{i=1..N}$. Those data were finally assembled in a KMC simulation scheme with a primary goal of reproducing observations and subsequently to extend it to more general conditions. The main simplification was geometric: all tissues were regular and designed based on the repetition of a same stem cell as illustrated in Figure 6 and described in section "Common assumptions" of Materials and Methods. The generated "crystalline" structure facilitated the coding of periodic boundary conditions. Conversely, filling and lag-times involved in KMC simulations fitted the real distributions of mechanistic parameters and not only their average.

Geometric Parameters. All potatoes were cut along their transversal axis of elongation. The geometry of parenchyma cell was sampled over 14 parenchyma structures digitized in 3-D as reproduced in Figure 8. Apparent radii of cells were calculated from disks of similar cross-section areas by assuming that flow rates were conserved (see section "Oil transport"). This choice was consistent with theoretical

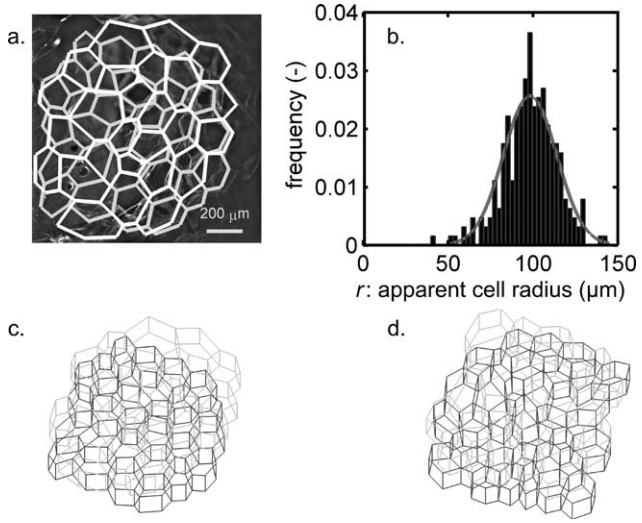

Figure 8. Typical reconstruction of 3-D cell arrangements in the potato crust from projected observations of Ref. 20.

(a) Digitized cell contours; (b) distribution of apparent cell radii, which preserve oil flow rate between hexagonal parenchyma cells and their cylindrical idealization; (c-d) 3-D reconstructions as an assembly of irregular prisms [assembly (c) corresponds to the tissue depicted in (a)].

descriptions of section "Finite volume effects" showing that viscous drag (proportional to cell circumferences) does not play any significant role. In this configuration, cell radii were found normally distributed with an average of 98 μm and with a standard deviation of 16 μm. From a statistical point of view, the symmetry of radii distribution around a same mean justified well our initial claim: averaging results over cells with different geometries yields to similar results as simulating an "averaged" cell. For common use, the stem radius was set to 100 μm in simulations, which corresponds also to the value reported in Ref. 92.

Oil–Air Front Displacements. It was not possible to identify and observe directly defects (holes, cracks, fissures...) used by oil to percolate from one cell layer to the next one. It was, nevertheless, inferred that the connection channel used to fill a cell of the second layer could not exceed half of the cell diameter, due to the shifted honeycomb arrangement of both layers (see Figures 6 and 8). Direct observations of oil percolation beyond the first cell layer were, however, scarce due to the difficulty of sampling large areas and due to the very low fraction of damaged cells in our experimental conditions. We recorded and reconstructed successfully 479 oil–air front positions, z, from dynamic 2-D images (see Eq. 17 and Supporting Information). The positions z should be envisioned at a cellular scale in a mean-field sense as they assumed a uniform filling across the section and ignored complex alternations of air and oil. Three typical observations are plotted in Figure 9. Their shapes match properly theoretical ones in presence of trapped bubbles and depicted in Figure 5. Because filling events of the first and second cell layers were separable, the displacements of oil–air front within each cell were fitted successively with Eq. 13 and by assuming $\varsigma = 0.95$ in Eq. 10 (first-order kinetic model). The agreement between theory and experiments was remarkable with a clear identification of an apparent lag-time due to a transient change in cross-section

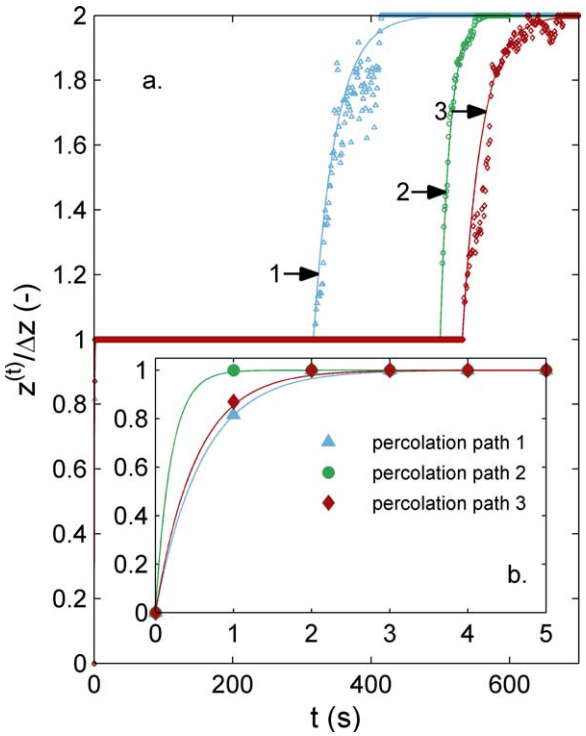

Figure 9. (a) Experimental oil–air front positions (symbols) long three percolation paths observed within the same parenchyma tissue and their comparisons with the micromodel (continuous lines fitted with Eq. 13). The inset (b) details the filling kinetics of the cells of the first cell layer during the first 5 s.

[Color figure can be viewed in the online issue, which is available at wileyonlinelibrary.com.]

(see Figure 5 for details of constriction effects) and with the verification of the inequality $\Delta t_{1,\mathrm{fill}} \ll \Delta t_{2,\mathrm{fill}}$. In details, triplets $\left(\Delta t_{1,\mathrm{fill}}, \Delta t_{2,\mathrm{lag}}, \Delta t_{2,\mathrm{fill}}\right)$ were of (2 s, 448 s, 97 s), (1 s, 825 s, 60 s), and (2 s, 962 s, 151 s), respectively for percolation paths 1, 2, and 3. The likely size of defects corresponding to kinetics in Figure 9 was guessed to 4 μm ± 1 μm from Eq. 16. The small size of defects could explain why they could not be identified from a priori observations.

As expected from the power four dependence to defect size in Eq. 15, kinetic parameters tended to be broadly and skewed distributed. The fitted and reconstructed kinetics corresponding to different classes of values of $\Delta t_{1,\mathrm{fill}}$ and $\Delta t_{2,\mathrm{fill}}$ are plotted in Figure 10 from 75 independent experiments. They confirmed the reliability of previous reconstructions and conclusions whatever the size of the defects connecting the cells of the first and second cell layers. Time fluctuations of $z(t)$ positions were associated to variations of the optical properties across the section due to the biphasic flow (as expressed via eq. 1 of Supporting Information).

Kinetic Parameters. The distributions of collected $\Delta t_{1,\mathrm{fill}}$, $\Delta t_{2,\mathrm{lag}}$, and $\Delta t_{2,\mathrm{fill}}$ values are plotted in Figure 11 and compared with fitted Gamma distributions. Typical percentiles Gamma parameters are summarized in Table 2. The reader should be aware that Shannon's rule prevented to estimate small $\Delta t_{i,\mathrm{fill}}$ values far below the acquisition time. The distribution of $\Delta t_{1,\mathrm{fill}}$ values was consequently truncated to low values. The collection of observations was sufficient to validate the assumption of Gamma distributions for all considered time constants. As justified in section "Dynamic simulation of oil penetration front" from the mixing rules of Gamma distributions, shape parameters a_Γ are increasing with the number of layers crossed. It is important to keep in mind that to cross a new junction, oil needs to cross another junction and that the momentum equation is integrated over the whole oil column (see Eq. 3). As reported in Table 2, the small increase of a_Γ was unnoticed due to experimental uncertainties. Unlike a_Γ, the scale parameters b_Γ were related to the size of defects used by oil to penetrate each cell. In the first cell layer, the initial entrance was as large as the cell size ($r = r_0$ in Eq. 15) and b_Γ associated to $\Delta t_{1,\mathrm{fill}}$ was lower than 1 s. It was about two decades longer for $\Delta t_{2,\mathrm{fill}}$. The discrepancy can have two origins: (1) some air escape mechanisms hinder the penetration of oil (see Eq. 8) and/or (2) the passage of a narrow constriction limits the oil flux (see Eq. 15). Lag-times $\Delta t_{2,\mathrm{lag}}$ longer than $\Delta t_{2,\mathrm{fill}}$ suggested that both effects occurred simultaneously with trapped bubbles causing an additional reduction of the passage section during a significant period of time (Eq. 16). By assuming that air was perfectly compressible, the continuous distribution of increments $\Delta t_{2,\mathrm{fill}} - \Delta t_{1,\mathrm{fill}}$ (introduced in Eq. 15) was inverted to infer the likely distribution of defect radii. It led to an almost symmetric distribution of r_0 centered on 3.8 μm (Figure 11d). By assuming as a mild guess that trapped bubbles were released when $\upsilon = 3\%$ of the next cell was filled with oil, average obstruction factor ξ induced by trapped bubbles was estimated to 0.29 from Eq. 16.

Time homogenization from isolated observations at cellular scale

Principles. Distributed values of $\Delta t_{1,\mathrm{fill}}$, $\Delta t_{2,\mathrm{lag}}$ and $\Delta t_{2,\mathrm{fill}}$, inferred from Figure 11, were generalized to $N > 2$ layers via the recurrence relationship (16) in conditions close to those met in,[20] when all cells are initially filled with air. Continuous distributions parameterized in Table 2 were preferred to experimental ones because they gave access to tail values. The analysis addressed here must, however, not be seen as a simple generalization of capillary migration to capillaries longer than two as it requires to devise percolation rules. Oil percolation from one cell to one of the three cells beneath was said possible when both cells were tagged as "damaged," which could be translated as connected through a defect. The type and size of defects were captured by the distributions of $\left\{\Delta t_{i,\mathrm{lag}}, \Delta t_{i,\mathrm{fill}}\right\}_{i=1..N}$ and introduced within the conventional KMC methodology [see algorithm (21)] to conduct dynamic simulations. By denoting d_i the probability to have a cell damaged in layer i, the probability to have given percolation path to extend to next layer was for a regular honeycomb (see Figure 6)

$$pr(\text{propagate a percolation path } i \rightarrow i+1) = p(d_{i+1}) = 3d_{i+1}(1-d_{i+1})^2 + 3d_{i+1}^2(1-d_{i+1}) + d_{i+1}^3 = 3d_{i+1} - 3d_{i+1}^2 + d_{i+1}^3 \quad (24)$$

The propagation of a percolation path from one layer to the next one was very likely only when $d_{i+1} \rightarrow 1$ and decreased proportionally to d_{i+1} when $d_{i+1} \rightarrow 0$. In experiments of,[20] only the value of d_1 was known and equal to 1 (all cells are cut and, therefore, fillable). As only few percolation paths were propagated to Layer 2, d_2 was thought to be low but remained unknown. A systematic study of nonlinear effects of $\left\{d_i\right\}_{i=1..n_{\mathrm{layers}}}$ was devised by simulating

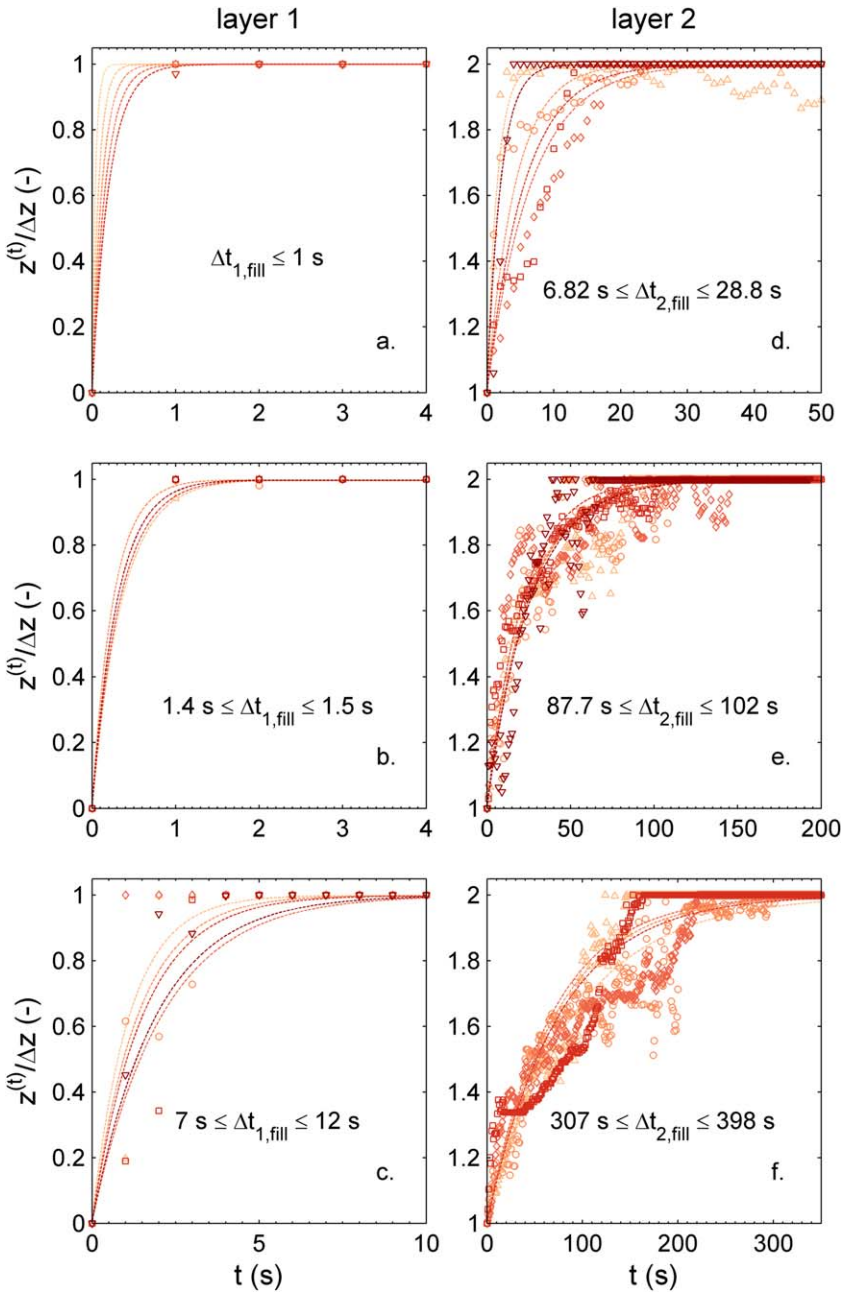

Figure 10. Oil–air front displacements in cells of Layer 1 (a–c) and Layer 2 (d–f). The 479 kinetics (75 experiments) are presented for the shortest (a,d), intermediate (b,e), and longest (c,f) filling times.

Symbols are experimental vlues and continuous lines are fitted with the micromodel (Eq. 13). [Color figure can be viewed in the online issue, which is available at wileyonlinelibrary.com.]

percolation routes for three-layer parenchyma structures obeying to the damage profile [1 d d]. Comparatively to reported experiments in Figure 10, adding one layer enabled to estimate the conditional probabilities to have a cell of layer $i+1$ filled when only some cells of layers i are filled. In this scenario, all damaged cells of Layer 2 were filled with oil at equilibrium. The probability to have any cell of Layer 3 also filled with oil at equilibrium was $d(3d-3d^2+d^3)$, which corresponded to the approximations $3d^2$and d in 0 and 1, respectively.

Static Oil Distribution at Tissue Scale. Oil distributions at equilibrium matching the damage profiles [1 d d] are illustrated in Figure 12a for some particular d values and plotted in Figures 12b,c for d varying continuously from 10^{-6} up to 1. To make details discernible, honeycomb structures exemplified in Figure 12a are 90 times smaller than those used for production. The fraction of cells filled with oil and the frequency of connected cells with the outside were particularly analyzed. Results were averaged over 10 parenchyma tissues with tiling radii of 100 cells. Averaged filling values converged rapidly to theoretical ones for infinite regular honeycombs, that are: d^0, d^1, and $3d^2$ respectively for the first, second, and third layer. The sharp decrease in oil content for intermediate d values is particularly consistent with prior observations of Ref. 17. The probability of a percolation route of length N decreased as expected as d^N. However, for

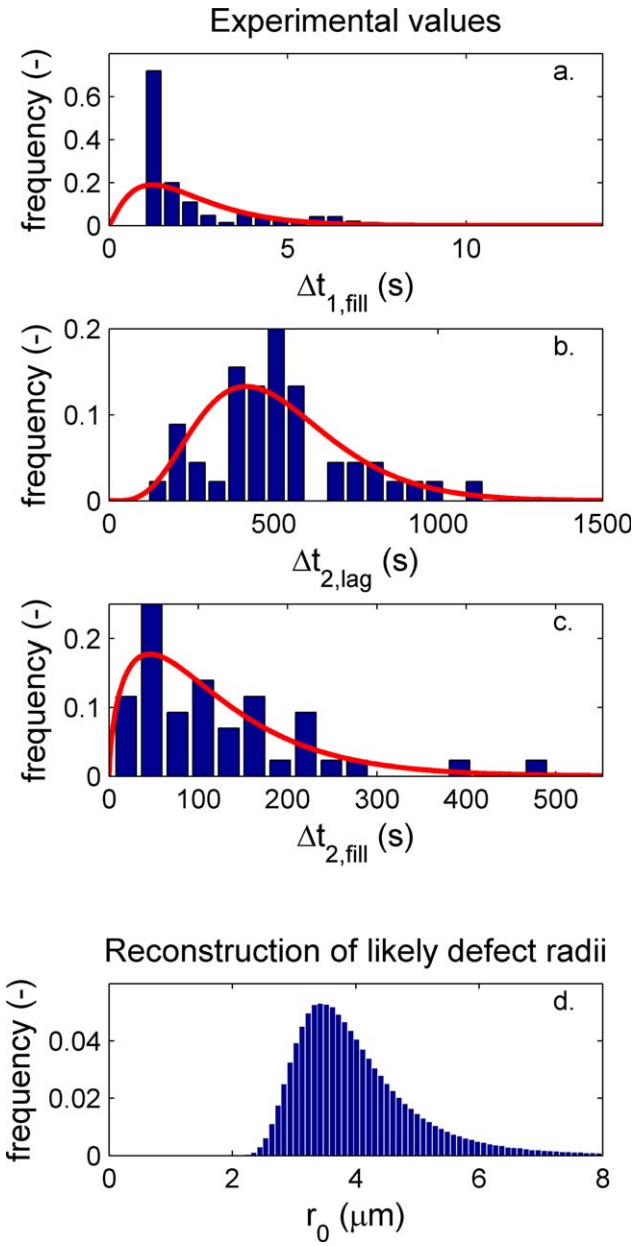

Figure 11. Distributions of $\Delta t_{1,\text{fill}}$ (a), $\Delta t_{2,\text{lag}}$ (b), and $\Delta t_{2,\text{fill}}$ (c). The likely distribution of the radii r_0 leading to $\Delta t_{2,\text{lag}}$ and $\Delta t_{2,\text{fill}}$ values are given in (d) (based on the micromodel set by Eq. 1515).

[Color figure can be viewed in the online issue, which is available at wileyonlinelibrary.com.]

$d \leq 10^{-4}$, the simulated tissue was too small to reproduce good statistics.

Dynamic Simulation of Oil Uptake at Tissue Scale. Static properties validated the feasibility of fast simulations at the scale of thousands cells using cell connectivity and distributions of cell damages. Dynamic simulations extended static ones by sampling continuously percolation time by deciding when the filling of each cell started and at which rate. All kinetics followed Eq. 13 with $\varsigma=0.9$. The process was repeated many times for randomly picked percolation routes, filling, and lag-times. Typical oil front positions sampled along three oil routes of length 3 are depicted in Figure 13a. Kinetics obtained were highly consistent with the complete model (6) illustrated in Figure 5. For 10^4 routes or more, a statistically correct oil front position is inferred. A sampling independent of the considered tissue was achieved by averaging results over more than 10 honeycomb structures. The distributions of $\{\Delta t_{i,\text{fill}}\}_{i=1..2}$ and $\{\Delta t_{i,\text{lag}}\}_{i=1..2}$ were identical to those reported in Table 2. The distributions of time constants for the third layer were inferred from Eq. 22, which led to: $a_\Gamma^{3,\text{fill}}=3.22$ and $a_\Gamma^{3,\text{lag}}=10.9$ with $b_\Gamma^{3,\text{fill}}=b_\Gamma^{2,\text{fill}}$ and $b_\Gamma^{3,\text{lag}}=b_\Gamma^{2,\text{lag}}$.

Several meaningful time and spatial averages (see Eq. 21) are plotted for different d values in Figures 13 and 14: oil saturation kinetics and oil profiles within each layer (Figures 13b,c) along the corresponding oil uptake kinetics at the scale of the whole tissue (Figure 14). Corresponding $\langle z^{(t)}\rangle$ and $\langle s^{(t)}\rangle$ values were averaged over cells belonging at least to one percolation route (i.e., filled with oil after some time) and over all cells in the honeycomb structure, respectively. In details, stair shapes dominated at the microscopic level whereas smooth trends were emerged at the macroscopic scale. At microscopic scale, oil front slow downed significantly after the passage of restrictions and almost stopped when air bubbles were transiently trapped inside. The connection probability with surface decreased approximately as $\begin{bmatrix}1 & d & 3d^2\end{bmatrix}$ forcing the saturation profiles to be discontinuous between layers. The oil saturation in the tissue was found consistently converging to its theoretical value $(1+d+3d^2)/3$. As expected, the simulated honeycomb structure reproduced a threshold of bond percolation of 1/3 (solution of $d=3d^2$) matching the coordination numbers in cells in z direction. Above this value, invasion percolation was possible and the same oil saturation value could be propagated from Layer 2 to Layer 3 enabling a continuous oil profile. Below this value, the saturation profile was sharply discontinuous although a same damage ratio was applied to Layers 2 and 3. Additional inhomogeneities were created by introducing lag-times between filling kinetics. They were responsible for the wavy shape of oil uptake kinetics (Figure 14b). As observed in Ref. 20, $\Delta t_{2,\text{lag}}$ led to a full separation of filling kinetics of Layers 1 and 2. KMC simulations showed that the conclusion did not hold beyond Layer 2 as $\Delta t_{3,\text{lag}}$, $\Delta t_{2,\text{fill}}$, and $\Delta t_{3,\text{fill}}$ reached similar magnitude orders with partly overlapping distributions. In particular, the simultaneous filling of Layers 2 and 3 made the average displacement of oil front more regular.

Alike dripping procedures in common frying practices, the simulated tissue remained covered with an excess of oil so that oil pickup was significantly overestimated for similar cell damages. However, some important features were expected to be well reproduced: the deep oil penetration occurred on time scales much longer than the oil surface invasion. This effect was mainly a consequence of mass conservation effects through constrictions. Lag-times, when they existed, were conversely the consequence of the oil–air counter-current configuration.

Extending KMC simulations to realistic post-frying conditions

Common Assumptions. Real products are not expected to exhibit homogeneous damages across layers as used in previous simulations. In our simulation framework, the attribute "damaged cell" covered several aspects: (1) the connectivity of cells enabling oil to pass from one cell layer to the next

Table 2. Gamma Distribution of Filling and Lag-Times Used in Kinetic Monte-Carlo Simulations Depicted in Figures 13 and 14

Kinetic parameter	Percentiles 5th	Percentiles 50th	Percentiles 95th	Fitted parameters[a] ± 95% confidence intervals: Shape parameter a_Γ (-)	Fitted parameters[a] ± 95% confidence intervals: Scale parameter b_Γ (s)	Mean $a_\Gamma b_\Gamma$ (s)	Standard-deviation $\sqrt{a_\Gamma} b_\Gamma$ (s)
$\Delta t_{1,\mathrm{fill}}$ (s)	<1	1.32	6.50	2.18 ± 0.405	1.03 ± 0.213	2.25	1.52
$\Delta t_{2,\mathrm{lag}}$ (s)	203	501	939	5.44 ± 2.21	93.9 ± 40.2	511	219
$\Delta t_{2,\mathrm{fill}}$ (s)	19.8	90	307	1.63 ± 0.625	72.6 ± 32.6	118	92.7
r_0 (μm)	2.65	3.55	5.63	–	–	3.78	1.02

[a]see Eq. (31).

one and (2) the size of defects at junctions r_0 or cell walls controlling the kinetic of penetration (see Eq. 15). According to Ref. 109, par-fried French-fries would be characterized by higher cellular damages, which should be translated as higher r_0 values than those assessed in Ref. 20 on carefully microtomed tissues. Achir et al.[17] showed, additionally, that the frequency of cells filled with oil was decreasing for cells initially filled with starch. As a result, the damage ratio d introduced in our KMC simulations had a meaning of "fillable with oil" regardless the cell is filled with starch or really damaged.

Previous simulations relied on experimental estimations of $\{\Delta t_{i,\mathrm{fill}}\}_{i=1..N}$,[20] their extension to more general cases required a direct estimation of these parameters and of their distributions. Typical $\Delta t_{1,\mathrm{fill}}$ values reported in Table 2, around 1 or 2 s, were an acceptable guess for a multipurpose application of our simulation framework. Conversely, a median value of $\Delta t_{2,\mathrm{fill}}$ around 70 s at 120°C seemed to be a dramatic overestimate. Generic simulations were conducted by assuming a value for $\langle r_0 \rangle$, which was increased 1.6 times up to 6 μm and corresponding to $\langle \Delta t_{2,\mathrm{fill}} \rangle \approx 10$ s. All subsequent quantities, including distribution parameters of $\{\Delta t_{i,\mathrm{fill}}\}_{i=1..N}$, were inferred from Eqs. 15 and 22. The principles were applied to $N = 4$ potato tissue, as reported in Table 3. Two average damage ratios (0.25 and 0.4) were considered on either side of the percolation threshold and simulated for three damage profiles (shown in Figure 16a) having: (1) a "V" shape profile with decreasing damages with depth, (2) a "flat" profile with uniform damage, and (3) a "hat" profile with increasing damages. As discussed in Ref. 18, the "V" shape and "hat" profiles are typical of cellular damage in fresh and par-fried French-fries. Without loss of generality, temperature gradients were neglected and both oil and tissue temperatures were assumed equal to 120°C. Oil uptake was assumed to occur without a significant contribution of air: $\{\Delta t_{i,\mathrm{lag}} = 0\}_{i=1..N}$ (no trapped bubbles), $\varsigma = 0.1$ (almost constant oil front penetration rate within each cell).

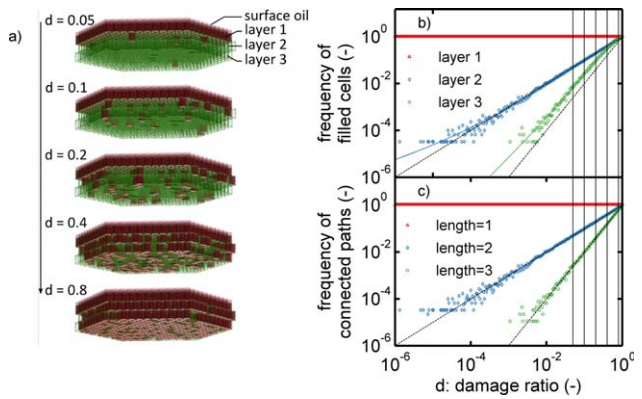

Figure 12. Distributions of oil at equilibrium in $N = 3$ layers tissues with damage profiles matching the pattern [1 *d d*]: (a) Tissue details (green = cell walls, red = oil); (b-c) Statistical analysis based on 250 tissues (3×10^4 cells each).

[Color figure can be viewed in the online issue, which is available at wileyonlinelibrary.com.]

Oil Distribution at Equilibrium. The equilibrium of oil distribution corresponding to Table 3 is plotted in Figures 15b,c. Values were calculated on tissues with a radius including 100 cells and averaged over 20 random tissues. All results converged rapidly toward theoretical expectations. A reasoning similar to Eq. 24 for the probability of filling one cell from the three cells above leads to the following recurrence relationship for oil saturation at equilibrium, denoted s_n^{eq}

$$s_n^{\mathrm{eq}} = p\left(s_{n-1}^{\mathrm{eq}}\right) d_n = \left[3 s_{n-1}^{\mathrm{eq}} - 3\left(s_{n-1}^{\mathrm{eq}}\right)^2 + \left(s_{n-1}^{\mathrm{eq}}\right)^3\right] d_n \text{ with } s_0^{\mathrm{eq}} = 1 \tag{25}$$

Oil concentration profiles were decreasing with depth while the condition $d_n < \frac{s_{n-1}^{\mathrm{eq}}}{p\left(s_{n-1}^{\mathrm{eq}}\right)}$ was fulfilled, which corresponded to a critical value of 0.5 at the threshold of percolation $s_n^{\mathrm{eq}} = 1/3$. As $p\left(s_{n-1}^{\mathrm{eq}}\right)$ was both lower than 1 and increasing with s_{n-1}^{eq}, oil saturation decreased more sharply than d_n: a small reduction of cellular damage had a stronger effect on oil uptake. In details, "hat" and "V" shapes exhibited a cross-over between the third and fourth layer. For a similar average damage ratio, "hat" shape profiles were more effective to reduce oil uptake. At relatively high damage ratios ($d_n > \frac{s_{n-1}^{\mathrm{eq}}}{p\left(s_{n-1}^{\mathrm{eq}}\right)}$), oil profile inversion was evidenced (Figures 15a,b), suggesting that oil could accumulate in large internal cavities while being supplied by a small number of open/damaged cells at the surface. This situation has been particularly observed in par-fried products.[18]

Oil Invasion Dynamics. As $\{\Delta t_{i,\mathrm{fill}}\}_{i=1..N}$ values were increasing with N, there was a synergetic effect between the profile shape and the average damage ratios. These effects are summarized in Figure 16. Oil uptake decreased sharply with depth below the threshold of percolation (Figure 16a). Comparatively to previous simulations, oil uptake kinetics were considerably faster and exhibited a pseudo exponential shape but without being homothetic with the final oil uptake value (Figure 16b). While the same kinetic parameters were applied to all the six simulated conditions, they could not be merged into one single master curve. Above the threshold of percolation, the hat shape caused in particular an inflection point around 30 s. The sensitivity to damages was greater for "V" and flat profiles but surprisingly low for "hat" profiles, which mimicked industrial par-fried products. Kinetics obtained with the "V" shape damage profile were highly

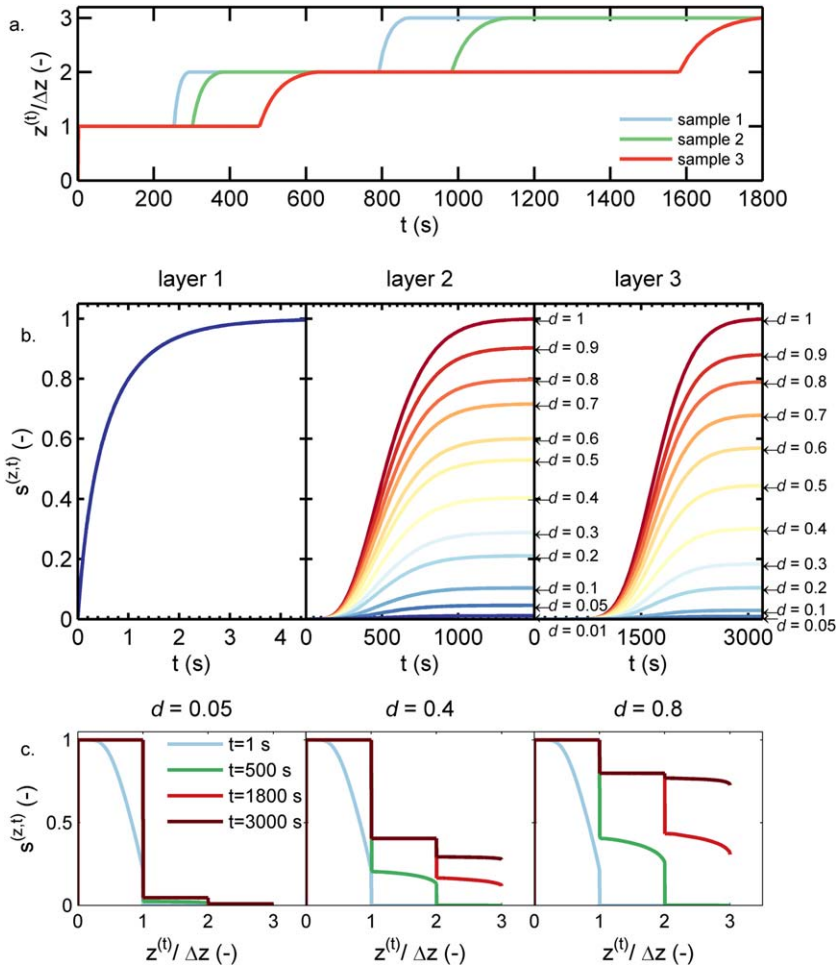

Figure 13. Simulated oil uptake within a $N = 3$ layers tissue with a damage profile [1 *d d*] and kinetic parameters detailed in Table 2: (a) typical oil position fronts; (b) filling kinetics of each layer; (c) oil saturation profiles for three typical *d* values.

[Color figure can be viewed in the online issue, which is available at wileyonlinelibrary.com.]

consistent with the kinetics obtained on products without cellular structure such as tortilla chips.[14,110] The highest resilience of the "hat" profile comes from the larger number of cells/cavities, which are not connected to the external surface.

Comparison with a diffusive model

Results of Figure 16a showed that microscopic kinetic parameters and microscopic structure ones were intimately intricate and could not be separated easily. In the continuum mechanics framework, both effects were conventionally captured with the concept of oil permeability. In multiphase flow in porous media, this effective transport property was replaced by the product of an absolute permeability, assessed with oil alone, and a relative one (dimensionless) affected by the local fluid composition (i.e., presence of steam/air, water). As both quantities are usually unknown for a material, whose composition and connectivity of pores depend on prior transformations (par-frying, freezing, finish-frying), it is convenient to replace the generalized Darcy multiphasic law by an equivalent diffusive process with an oil diffusion coefficient varying with oil concentration. These simplifications have been reviewed in Ref. 20 (see section "Practical approximations of Eqs. 6 and 8 for individual cells") based on the work of Ref. 10. Although they relied on different grounds, our KMC simulations involved also an effective diffusion coefficient $D_o(T) = \frac{r\gamma(T)\cos(\theta)}{8\eta_{oil}(T)}$ (see Eq. 15) capturing the Poiseuille flow assumption (see Eq. 11). It is worth noticing that when a significant gradient of gas pressure exists, the previous apparent diffusion coefficient can be augmented by the pressure gauge, as $D_o(T) = \frac{r\gamma(T)\cos(\theta) + r^2(P_{atm} - P_{air}(t,T))}{8\eta_{oil}(T)}$.

Phenomenologically, Halder et al.[10] introduced an effective diffusion coefficient, which was increasing exponentially with oil saturation. In our terms, the authors described an increase of filling times, which tend to increase deep beneath the surface (in regions not wet by oil in fact) in a close fashion as Eq. 15 does. Diffusion-like profiles were consistent with flat and "V" shape damage profiles (see Figure 16a) and offered enough incentive for a crude comparison between our KMC approach and the continuous mechanics approach. In absence of detailed simulations on potato products, numerical simulations on tortilla chips[11] and parameterized on experimental values of Ref. 110 were chosen as reference. Fried tortilla chips are very porous materials ($\varepsilon = 0.928$), showing 100% expansion in the central region (see figure 5 of Ref. 110). For this comparison and due to the

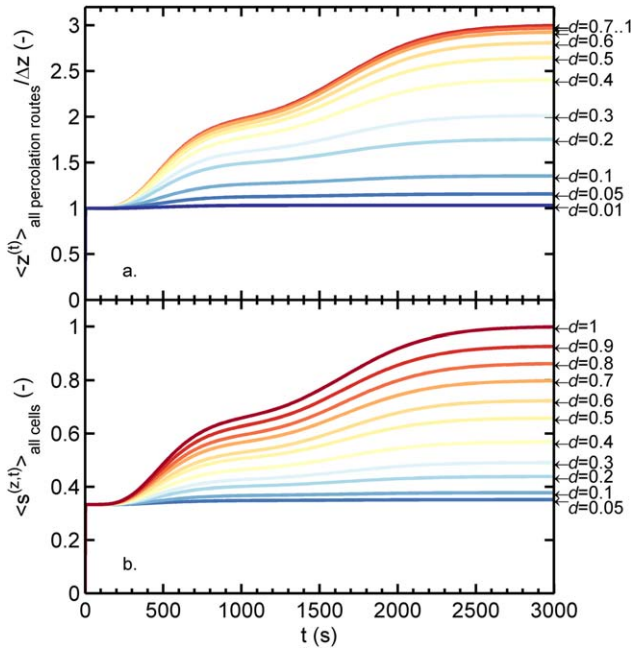

Figure 14. Oil penetration front (a) and oil saturation kinetics (b) corresponding to Figure 13.

[Color figure can be viewed in the online issue, which is available at wileyonlinelibrary.com.]

absence of cellular structure, our KMC simulation framework should be thought as a cellular automata mapping space via connected "tubes." The following damage profile was therefore considered [d_0 d d d...] with $N = 11$. The value d_0 was introduced to enforce the arbitrary boundary conditions used by authors ($d_0 = 0.28$). A reasonable value of $d = 0.4$ was chosen so that the saturation profile was slightly decreasing with depth at equilibrium. According to Eq. 25, a value of $d = 0.447$ would have yielded to a flat profile. Kinetic parameters were chosen close to those listed in Table 3: $\left\{a_\Gamma^{i,\mathrm{fill}}\right\}_{i=1..2} = [2, 3]$, $b_\Gamma^{1,\mathrm{fill}}{}_{i=2..11} = 1$ s, $\left\{b_\Gamma^{i,\mathrm{fill}}\right\}_{i=2..11} = 2.5$ s, with an increment $a_\Gamma^{i+1,\mathrm{fill}} - a_\Gamma^{i,\mathrm{fill}} = 2.2$ for i=2..10 corresponding to a constriction passage between cylindrical volumes ($r = 100$ μm, $\Delta z = 350$ μm) of 6.6 μm [see recurrence relationship (23)]. Our simulated results are compared with Halder et al. ones[11] in Figure 17, for equivalent post-frying conditions. It is worth noticing that the model of Ref. 11 predicted a significant oil transfer during immersion frying, which was not considered in our case.

Without significant adjustments of input parameters comparatively to previous simulation cases in this study, our KMC simulations showed a good agreement with the oil saturation profiles (Figure 17a), the average position of the oil front, denoted $\langle z^{(t)} \rangle$ (Figure. 17b) and oil content (Figure 17c). The scaling of $\langle z^{(t)} \rangle$ with time was further analyzed as

$$\langle z^{(t)} \rangle_{\text{all cells}} = \int_0^{+\infty} z\left(s^{(t,z)} - s^{(t=0,z)}\right) dz \Big/ \int_0^{+\infty} \left(s^{(t,z)} - s^{(t=0,z)}\right) dz \approx Bt^{\alpha} \tag{26}$$

where B is a scaling constant and α a scaling exponent measuring the compactness of the oil invasion process at spanning times. Both α values were closely related: 0.45 ± 0.03 and 0.49 ± 0.02, for our simulations and Halder et al. ones[11] respectively. Removing the first layer ($d_0 < d$) improved the agreement with the theoretical value of 0.5 corresponding to oil front displacements within a tube with uniform section under the sole influences of capillary forces and drag flows (see Eq. 9 without momentum variation). In this perspective, the quantities d and d_0 in our cell automata did not represent the porosity of the material but the volume fractions, which were potentially accessible to oil from the outside. Conversely, $\varepsilon - d \approx 0.5$ represented voids, which were initially filled by puffed gelatinized starch, air bubbles, residual liquid water (or steam) and which could not be invaded by oil due to topological constraints (trapped volumes) or due to strong viscous drags. This interpretation is consistent with the relatively low oil saturation at the interface (0.28) in a highly porous material ($\varepsilon = 0.928$). Values of d larger than 0.5 would have caused fractal oil flows with protuberances close to the surface and with internal bulk reservoirs. These effects could not be reproduced with the approximations used in Ref. 11, which consider only Fickian-like diffusion. Non-Fickian diffusion with apparent oil transport from low to high saturated regions is described in Figures 15 and 16 with the "hat" damage profiles. They are made possible not because the underlying physics would be different (capillary is the main driving force in both cases) but because the microscopic approach relates on the effective diffusion coefficient and the effective oil capacity to the local structure and not to the local oil content. All these aspects are considered explicitly in the proposed KMC formulation.

Table 3. Parameters Used to Simulate Oil Uptake Within a $N = 4$ Tissue Subjected to Damage Profiles with "V", "Flat," and "Hat" Shapes

		Damage ratio: d (same average $< d >$)			$\Delta t_{i,\mathrm{fill}} \sim \Gamma(a_\Gamma^{i,\mathrm{fill}}, b_\Gamma^{i,\mathrm{fill}})$		
Damage level	Layer	"V"	"Flat"	"Hat"	$a_\Gamma^{i,\mathrm{fill}}$ (-)	$b_\Gamma^{i,\mathrm{fill}}$ (s)	Cumulated mean filling time (s) $\sum_{i=1}^{i'} a_\Gamma^{i,\mathrm{fill}} b_\Gamma^{i',\mathrm{fill}}$
High	1	0.7	0.4	0.1	2.0	1.0	2.0
	2	0.5	0.4	0.3	3.0	3.5	13
	3	0.3	0.4	0.5	5.4	3.5	31
	4	0.1	0.4	0.7	7.9	3.5	59
Mean $< d >$		0.4	0.4	0.4	–	–	–
Moderate	1	0.4	0.25	0.1	2.0	1.0	2.0
	2	0.3	0.25	0.2	3.0	5	13
	3	0.2	0.25	0.3	5.4	5	31
	4	0.1	0.25	0.4	7.9	5	59
Mean $< d >$		0.25	0.25	0.25	–	–	–

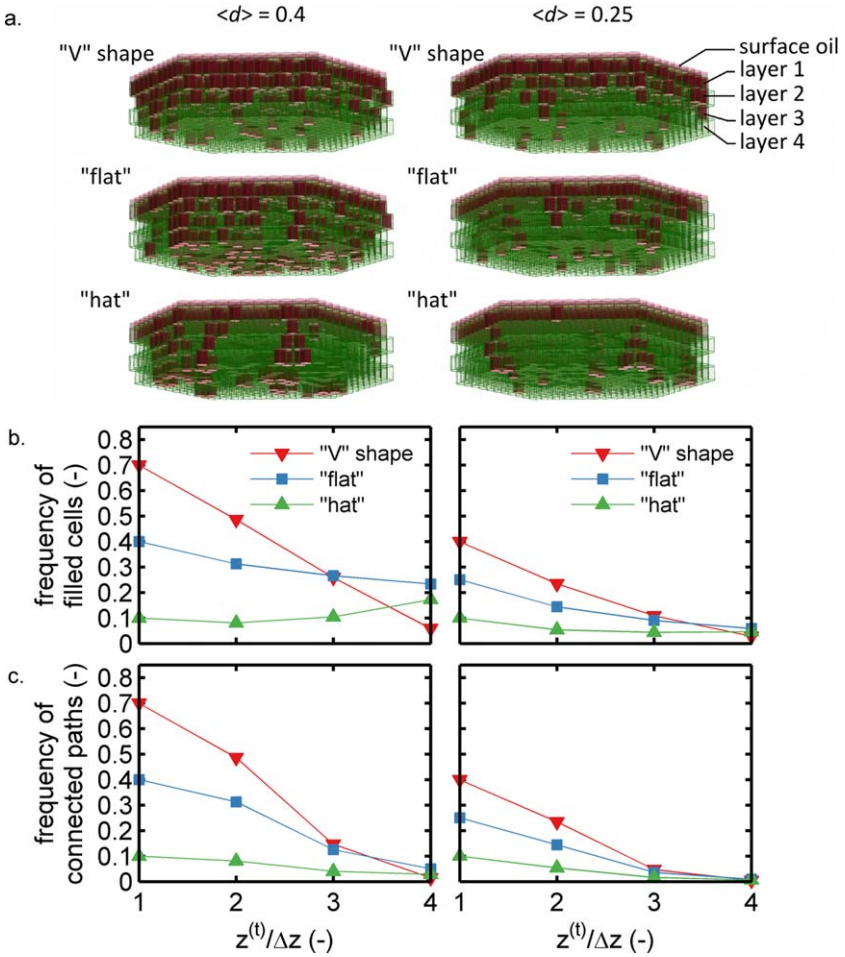

Figure 15. Distributions of oil at equilibrium in $N = 4$ layers tissues (3×10^4 cells each) with damage profiles listed in Table 3. Tissue details (green = cell walls, red = oil) are depicted in (a) with corresponding statistical analysis plotted in (b-c).

[Color figure can be viewed in the online issue, which is available at wileyonlinelibrary.com.]

Conclusions

A general framework based on Kinetic Monte-Carlo (KMC) simulations coupled with a first-passage algorithm has been devised to describe oil uptake at the cellular scale in presence or not of an incondensable phase. The proposed KMC scheme uses filling and lag-times instead of conventional effective transport properties to describe oil uptake. These properties can be directly measured from microscopic experiments or derived from the suggested oil–air flow micromodel. It has been shown that the micromodel predicted a very similar separation of time scales when several cell layers were successively invaded as observed in Ref. 20. As a result, the KMC approach mimics, in essence, the heterogeneous dynamics of oil invasion between cells arranged as honeycomb and connected through narrow constrictions. Recurrence relationships were established between filling and lag-times as well as their distributions in values to extend the predictions beyond the initial observation ranges. In agreement with the micromodel and observations, lag-times are specifically interpreted as the consequence of bubbles trapped in defects. They reduce temporarily the passage diameter and, consequently, the oil flow rate.

Oil uptake has been simulated in various conditions by assuming a regular 3-D parenchyma structure and a gradient of a parameter so-called cell damage. This quantity is

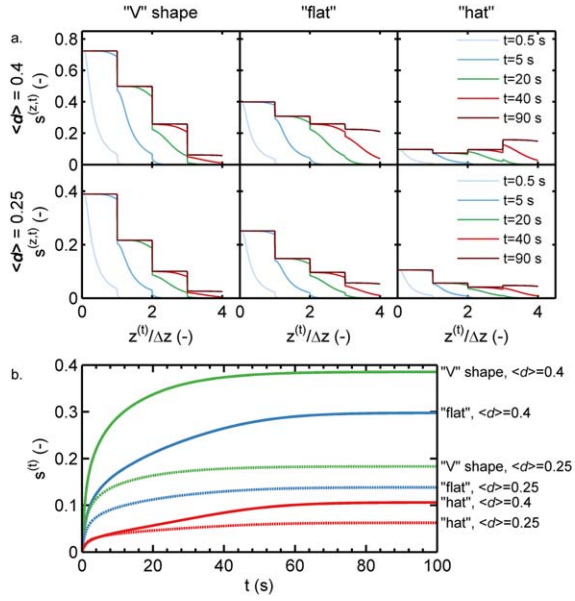

Figure 16. (a) Oil saturation profiles and (b) oil uptake kinetics in $N = 4$ layers structure described in Table 3.

<d> denotes the average damage ratio. [Color figure can be viewed in the online issue, which is available at wileyonlinelibrary.com.]

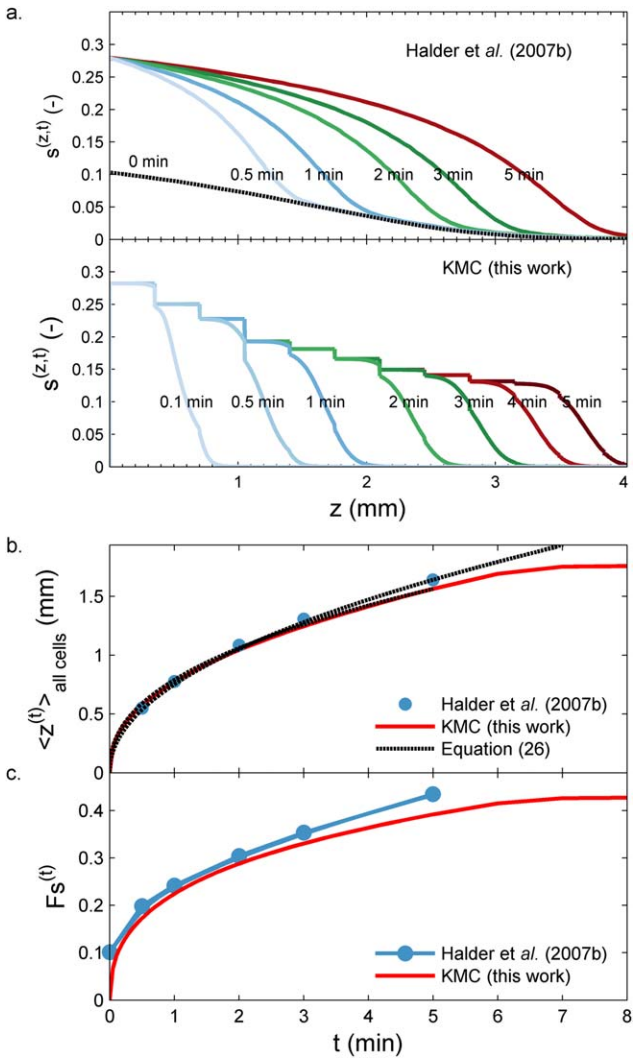

Figure 17. Comparison of KMC results (this work, $N = 12$ layer tissue) with simulations of Ref. [11]: (a) oil saturation profiles, (b) average oil position (see Eq. 2526), (c) kinetics of oil uptake.

[Color figure can be viewed in the online issue, which is available at wileyonlinelibrary.com.]

generic and represents the quality of a cell to be fillable with oil either because it is damaged or because the corresponding oil route is not obstructed by another phase: water, dry gelatinized starch. Periodic boundary conditions in the product surface plane granted simulated results with a fast and reliable convergence to theoretical ones at an infinite time. It is shown that final oil pickup was not a direct function of porosity but depended in a complex manner on the amount of oil available at the surface, on the connectivity of damaged cells and on the size of passage sections. The methodology enabled the investigation of phenomena distributed on broad time scales, from 10^{-4} s to 10^{4} s, in highly heterogeneous tissues with random connections between cells. In particular, it is shown that surface oil uptake is a fast process due to the large opening of cells and the relatively short length of cells. By contrast, filling times increase dramatically with depth due to a percolation fed through a series of small defects (passages) connecting cells. The typical invasion time increases with the square length of the percolation route and increases linearly with the number of constrictions crossed. Trapped air bubbles can make the dynamics additionally more chaotic. Combined with the strong viscosity of oil at room temperature, this general phenomenon should block the redistribution of oil after frying. Calculations showed that passage radii shorter than 1 μm could almost block deep oil penetration. This effect would also explain why dry porous starch is a very good barrier to oil.

Regardless the impregnated material comprised a cellular structure, it has been demonstrated that KMC simulations fed with correct filling times and "damage ratios" give time scales and oil uptake values very comparable to detailed mechanistic models. The superiority of KMC and first-passage models arises from their 3-D representations integrating main structural and organization properties of the biological material, while keeping calculations fast (few minutes to few hours on a single processor) and a few number of initial inputs. As most of the properties can be inferred recursively, minimalist parameterizations require only surface kinetic parameters. The integration of process conditions requires two significant refinements: (1) coupling with heat transfer and (2) limiting the amount of oil available at the product surface. In particular, evaporation or condensation could be implemented via the drying algorithm reviewed in Ref. 111. Future works will be devoted to make these developments available as an open-source project and to simulate oil uptake in real structures digitized by micro-computed X-ray tomography.

Acknowledgments

The authors gratefully acknowledge the DISCO beamline team of synchrotron SOLEIL for supporting this study (Proposal 20110137) and "Association Nationale de la Recherche et de la Technologie" (ANRT) agency for co-funding the study. The authors would like to thank also the group McCain, which made this study possible.

Notation

B = scaling constant in Eq. 26
d = cell defect ratio
F_s = oil content respectively to the non-fat solid content, kg oil kg^{-1} solid
Fo_C = "capillary" Fourier number
g = acceleration of gravity, m s^{-2}
L_{max} = capillary length in Eq. 1, m
l_i = length of the ith cell in a sequence, m
m = mass of oil filling the tube or cells, kg
N = number of cell layers
P_{air} = pressure of air in tube or cell, Pa
P_{atm} = atmospheric pressure, Pa
p_c = capillary pressure, Pa
r = effective radius, m
r_i = radius of the ith cell in a sequence, m
s = oil saturation
T = temperature, K
t = time, s
$\Delta t_{i,fill}$ = filling time of the ith cell in a sequence, s
$\Delta t_{i,lag}$ = lag-time before entering in the ith cell in a sequence, s
v = oil–air velocity front, m s^{-1}
z = radially averaged oil front position, m
z_{bottom} = position of the bottom of the considered cell, m
Δz = cell length, m

Greek Symbols

α = scaling constant used in Eq. 26
$\alpha_{counter}$ = air escape constant in counter current flow mechanism (see Eqs. 8 and 10), m^2 s^{-1}

α_{piston} = air escape constant in piston flow mechanism (see Eqs. 8 and 10), ms^{-1}
$\alpha_{transpiration}$ = air escape constant in transpiration flow mechanism (see Eqs. 8 and 10), s^{-1}
ε = apparent porosity of the parenchyma tissue
η_{oil} = dynamic viscosity of oil, Pa s
ϕ_{air} = air volume fraction
γ = oil–air surface tension, N m^{-1}
υ = ratio of cell length necessary to escape trapped bubble ($0 < \upsilon < 1$)
ρ_{oil} = oil density, kg m^{-3}
ρ_s = solid density, kg m^{-3}
$\Gamma(a_\Gamma, b_\Gamma)$ = Gamma function with shape parameter a_Γ and scale parameter b_Γ, s
θ = contact angle between solid matrix, oil and air, rad
ξ = hydraulic diameter reduction due to the presence of trapped bubbles in defects, used in Eq. 16
ζ = initial liquid height used in Eq. 6, m
ζ = shape factor in Eq. 13 ($0 < \zeta < 1$)

Literature Cited

1. Ufheil G, Escher F. Dynamics of oil uptake during deep-fat frying of potato slices. *LWT-Food Sci Technol*. 1996;29(7):640–644.
2. Moreira RG, Sun XZ, Chen YH. Factors affecting oil uptake in tortilla chips in deep-fat frying. *J Food Eng*. 1997;31(4):485–498.
3. Achir N, Vitrac O, Trystram G. Heat and mass transfer during frying. In: Sahin S, Sumunu SG, editors. *Advances in Deep-Fat Frying*. Boca-Raton: CRC Press, 2009:5–32.
4. Mehta U, Swinburn B. A review of factors affecting fat absorption in hot chips. *Crit Rev Food Sci Nutr*. 2001;41(2):133–154.
5. Moreira RG, Castell Perez ME, Barrufet MA. *Deep-fat frying: fundamentals and applications*. Gaithersburg, MD: Aspen Publishers, 1999.
6. Saguy IS, Ufheil G, Livings S. Oil uptake in deep-fat frying: review. *OCL*. 1998;5(1):30–35.
7. Yamsaengsung R, Moreira RG. Modeling the transport phenomena and structural changes during deep fat frying—Part 1: model development. *J Food Eng*. 2002;53(1):1–10.
8. Troncoso E, Pedreschi F. Modeling water loss and oil uptake during vacuum frying of pre-treated potato slices. *LWT-Food Sci Technol*. 2009;42(6):1164–1173.
9. Ni H, Datta AK. Moisture, oil and energy transport during deep-fat frying of food materials. *Food Bioprod Process*. 1999;77(C3):194–204.
10. Halder A, Dhall A, Datta AK. An improved, easily implementable, porous media based model for deep-fat frying—Part I: Model development and input parameters. *Food Bioprod Process*. 2007;85(C3):209–219.
11. Halder A, Dhall A, Datta AK. An improved, easily implementable, porous media based model for deep-fat frying—Part II: Results, validation and sensitivity analysis. *Food Bioprod Process*. 2007;85(C3):220–230.
12. Moreira RG, Barrufet MA. Spatial distribution of oil after deep-fat frying of tortilla chips from a stochastic model. *J Food Eng*. 1996;27(3):279–290.
13. Rajkumar V, Moreira R, Barrufet M. Modeling the structural changes of tortilla chips during frying. *J Food Eng*. 2003;60(2):167–175.
14. Moreira RG, Barrufet MA. A new approach to describe oil absorption in fried foods: a simulation study. *J Food Eng*. 1998;35(1):1–22.
15. Bouchon P, Pyle DL. Modelling oil absorption during post-frying cooling— I: model development. *Food Bioprod Process*. 2005;83(C4):253–260.
16. Bouchon P, Pyle DL. Modelling oil absorption during post-frying cooling—II: Solution of the mathematical model, model testing and simulations. *Food Bioprod Process*. 2005;83(C4):261–272.
17. Achir N, Vitrac O, Trystram G. Direct observation of the surface structure of French fries by UV-VIS confocal laser scanning microscopy. *Food Res Int*. 2010;43(1):307–314.
18. Vauvre J-M, Kesteloot R, Patsioura A, Vitrac O. Microscopic oil uptake mechanisms in fried products. *Eur J Lipid Sci Technol*. 2014;116(6):741–755.
19. Achir N, Vitrac O, Trystram G. Simulation and ability to control the surface thermal history and reactions during deep fat frying. *Chem Eng Process*. 2008;47(11):1953–1967.
20. Patsioura A, Vauvre JM, Kesteloot R, Jamme F, Hume P, Vitrac O. Microscopic imaging of biphasic air-oil flow in potato parenchyma structures using Synchrotron radiation. *AIChE J*. In press. doi: 10.1002/aic.14744
21. Buckley SE, Leverett MC. Mechanism of fluid displacement in sands. *Trans AIME*. 1942;146:107–116.
22. Kalogianni EP, Papastergiadis E. Crust pore characteristics and their development during frying of French-fries. *J Food Eng*. 2014;120(0):175–182.
23. Dullien FAL, El-Sayed MS, Batra VK. Rate of capillary rise in porous media with nonuniform pores. *J Colloid Interface Sci*. 1977;60(3):497–506.
24. Schoelkopf J, Gane PAC, Ridgway CJ, Matthews GP. Practical observation of deviation from Lucas–Washburn scaling in porous media. *Colloids Surfaces A*. 2002;206(1–3):445–454.
25. Patro D, Bhattacharyya S, Jayaram V. Flow kinetics in porous ceramics: understanding with non-uniform capillary models. *J Am Ceram Soc*. 2007;90(10):3040–3046.
26. Erickson D, Li D, Park CB. Numerical simulations of capillary-driven flows in nonuniform cross-sectional capillaries. *J Colloid Interface Sci*. 2002;250(2):422–430.
27. Liou WW, Peng Y, Parker PE. Analytical modeling of capillary flow in tubes of nonuniform cross section. *J Colloid Int Sci*. 2009;333(1):389–399.
28. Frank X, Perré P. The potential of meshless methods to address physical and mechanical phenomena involved during drying at the pore level. *Drying Technol*. 2010;28(8):932–943.
29. Henrich B, Cupelli C, Moseler M, Santer M. An adhesive DPD wall model for dynamic wetting. *Europhys Lett*. 2007;80(6):60004.
30. Tartakovsky AM, Ward AL, Meakin P. Pore-scale simulations of drainage of heterogeneous and anisotropic porous media. *Phys Fluids*. 2007;19(10):103301.
31. Frank X, Almeida G, Perré P. Multiphase flow in the vascular system of wood: from microscopic exploration to 3-D Lattice Boltzmann experiments. *Int J Multiphase Flow*. 2010;36(8):599–607.
32. Frank X, Perré P. Droplet spreading on a porous surface: a lattice Boltzmann study. *Phys Fluids*. 2012;24(4):042101.
33. van der Sman RGM. Investigation of Lattice Boltzmann wetting boundary conditions for capillaries with irregular polygonal cross-section. *Comput Phys Commun*. 2013;184(12):2751–2760.
34. Hatiboglu C, Babadagli T. Pore-scale studies of spontaneous imbibition into oil-saturated porous media. *Phys Rev E*. 2008;77(6):066311.
35. Succi S. The Lattice Boltzmann Equation: For Fluid Dynamics and Beyond. Oxford: Oxford University Press, 2001.
36. van der Sman RGM, Vergeldt FJ, Van As H, van Dalen G, Voda A, van Duynhoven JPM. Multiphysics pore-scale model for the rehydration of porous foods. *Innov Food Sci Emerg Technol*. 2014;24(0):69–79.
37. Štěpánek F, Rajniak P. Droplet Morphologies on Particles with Macroscopic Surface Roughness. *Langmuir*. 2006;22(3):917–923.
38. Blunt MJ. Flow in porous media—pore-network models and multiphase flow. *Curr Opin Colloid Interface Sci*. 2001;6(3):197–207.
39. Gillespie DT. Exact stochastic simulation of coupled chemical reactions. *J Phys Chem*. 1977;81(25):2340–2361.
40. Gibson MA, Bruck J. Efficient exact stochastic simulation of chemical systems with many species and many channels. *J Phys Chem A*. 2000;104(9):1876–1889.
41. Salis H, Sotiropoulos V, Kaznessis Y. Multiscale Hy3S: Hybrid stochastic simulation for supercomputers. *BMC Bioinform*. 2006;7(1):93.
42. Yortsos YC, Stubos AK. Phase change in porous media. *Curr Opin Colloid Interface Sci*. 2001;6(3):208–216.
43. Joekar-Niasar V, Hassanizadeh SM. Analysis of fundamentals of two-phase flow in porous media using dynamic pore-network models: a review. *Crit Rev Environ Sci Technol*. 2012;42(18):1895–1976.
44. Kaviany M. *Principles of Heat Transfer in Porous Media*, 2nd ed. Berlin: Springer-Verlag, 1997.
45. Pinder GF, Gray WG. *Essentials of Multiphase Flow in Porous Media*. Hoboken: Wiley, 2008.
46. Jacquin CG, Adler PM. The fractal dimension of a gas—liquid interface in a porous medium. *J Colloid Interface Sci*. 1985;107(2):405–417.
47. Loggia D, Bo Z, Xiaorong L, Vasseur G. Experimental study of upward oil migration in a fracture. *Transp Porous Med*. 2009;80(1):1–16.

48. Wilkinson D, Willemsen JF. Invasion percolation: a new form of percolation theory. *J Phys A*. 1983;16(14):3365.
49. Vidales AM, Miranda E, Nazzarro M, Mayagoitia V, Rojas F, Zgrablich G. Invasion percolation in correlated porous media. *Europhys Lett*. 1996;36(4):259–264.
50. Chandler R, Koplik J, Lerman K, Willemsen JF. Capillary displacement and percolation in porous media. *J Fuid Mech*. 1982;119:249–267.
51. Wilkinson D. Percolation effects in immiscible displacement. *Phys Rev A*. 1986;34(2):1380–1391.
52. Wilkinson D. Percolation model of immiscible displacement in the presence of buoyancy forces. *Phys Rev A*. 1984;30(1):520–531.
53. Hirsch LM, Thompson AH. Size-dependent scaling of capillary invasion including buoyancy and pore size distribution effects. *Phys Rev E*. 1994;50(3):2069–2086.
54. Hatiboglu C, Babadagli T. Diffusion mass transfer in miscible oil recovery: visual experiments and simulation. *Transp Porous Med*. 2008;74(2):169–184.
55. Deutsch S. A preliminary study of the fluid mechanics of liquid penetrant testing. *J Res Natl Bur Stand*. 1979;84(4):287–292.
56. Zhmud BV, Tiberg F, Hallstensson K. Dynamics of capillary rise. *J Colloid Interface Sci*. 2000;228(2):263–269.
57. Chibbaro S. Capillary filling with pseudo-potential binary Lattice-Boltzmann model. *Eur Phys J E*. 2008;27(1):99–106.
58. Hultmark M, Aristoff JM, Stone HA. The influence of the gas phase on liquid imbibition in capillary tubes. *J Fluid Mech*. 2011;678:600–606.
59. Fazio R, Iacono S. An analytical and numerical study of liquid dynamics in a one-dimensional capillary under entrapped gas action. *Math Methods Appl Sci*. 2014;37(18):2923–2933.
60. Vitrac O, Hayert M. Effect of the distribution of sorption sites on transport diffusivities: a contribution to the transport of medium-weight-molecules in polymeric materials. *Chem Eng Sci*. 2007;62(9):2503–2521.
61. Vitrac O, Hayert M. Risk assessment of migration from packaging materials into foodstuffs. *AIChE J*. 2005;51(4):1080–1095.
62. Vitrac O, Trystram G, Raoult-Wack AL. Deep-fat frying of food: heat and mass transfer, transformations and reactions inside the frying material. *Eur J Lipid Sci Technol*. 2000;102(8–9):529–538.
63. Bodurtha PA, Matthews GP, Kettle JP, Roy IM. Influence of anisotropy on the dynamic wetting and permeation of paper coatings. *J Colloid Interface Sci*. 2005;283(1):171–189.
64. Brielles N, Chantraine F, Viana M, Chulia D, Branlard P, Rubinstenn G, Lequeux F, Lasseux D, Birot M, Roux D, Mondain-Monval O. Imbibition and dissolution of a porous medium. *Indus Eng Chem Res*. 2007;46(17):5785–5793.
65. Culligan PJ, Barry DA, Parlange JY, Steenhuis TS, Haverkamp R. Infiltration with controlled air escape. *Water Resour Res*. 2000;36(3):781–785.
66. Mason G, Fischer H, Morrow NR, Ruth DW. Correlation for the effect of fluid viscosities on counter-current spontaneous imbibition. *J Petrol Sci Eng*. 2010;72(1–2):195–205.
67. Chen C, Gao C, Zhuang L, Li X, Wu P, Dong J, Lu J. A many-body dissipative particle dynamics study of spontaneous capillary imbibition and drainage. *Langmuir*. 2010;26(12):9533–9538.
68. Chen C, Zhuang L, Li X, Dong J, Lu J. A many-body dissipative particle dynamics study of forced water–oil displacement in capillary. *Langmuir*. 2011;28(2):1330–1336.
69. Morrow NR, Mason G. Recovery of oil by spontaneous imbibition. *Curr Opin Colloid Interface Sci*. 2001;6(4):321–337.
70. Li K. Scaling of spontaneous imbibition data with wettability included. *J Contam Hydrol*. 2007;89(3–4):218–230.
71. Cortés P, Badillo G, Segura L, Bouchon P. Experimental evidence of water loss and oil uptake during simulated deep-fat frying using glass micromodels. *J Food Eng*. 2014;140:19–27.
72. BeMiller JN, Whistler RL. *Starch: Chemistry and Technology*. New York: Elsevier Science, 2009.
73. Washburn EW. The dynamics of capillary flow. *Phys Rev*. 1921;17(3):273–283.
74. Hamraoui A, Nylander T. Analytical approach for the Lucas–Washburn equation. *J Colloid Interface Sci*. 2002;250(2):415–421.
75. Reyssat M, Courbin L, Reyssat E, Stone HA. Imbibition in geometries with axial variations. *J Fluid Mech*. 2008;615:335–344.
76. Ramon G, Oron A. Capillary rise of a meniscus with phase change. *J Colloid Interface Sci*. 2008;327(1):145–151.
77. Li Y, Mason G, Morrow NR, Ruth DW. Capillary pressure at a saturation front during restricted counter-current spontaneous imbibition with liquid displacing air. *Transp Porous Med*. 2011;87(1):275–289.
78. Joekar-Niasar V, Hassanizadeh SM. Pore-network modeling of wicking: a two-phase flow approach. In: Masoodi R, Pillai KM, editors. *Wicking in Porous Materials: Traditional and Modern Modeling Approaches*. Boca-Raton: Taylor & Francis, 2012:237–262.
79. Fenwick DH, Blunt MJ. Three-dimensional modeling of three phase imbibition and drainage. *Adv Water Resour*. 1998;21(2):121–143.
80. Lenormand R, Zarcone C, Sarr A. Mechanisms of the displacement of one fluid by another in a network of capillary ducts. *J Fluid Mech*. 1983;135(-1):337–353.
81. Ransohoff TC, Gauglitz PA, Radke CJ. Snap-off of gas bubbles in smoothly constricted noncircular capillaries. *AIChE J*. 1987;33(5):753–765.
82. Held RJ, Celia MA. Modeling support of functional relationships between capillary pressure, saturation, interfacial area and common lines. *Adv Water Resour*. 2001;24(3–4):325–343.
83. Robards AW, Lucas WJ. Plasmodesmata. *Annu Rev Plant Physiol Plant Mol Biol*. 1990;41(1):369–419.
84. Davison BH, Parks J, Davis MF, Donohoe BS. Plant cell walls: basics of structure, chemistry, accessibility and the influence on conversion. In: Wyman CE, editor. *Aqueous Pretreatment of Plant Biomass for Biological and Chemical Conversion to Fuels and Chemicals*. Chichester, West Sussex: Wiley, 2013:23–38.
85. Vidales AM, Riccardo JL, Zgrablich G. Pore-level modelling of wetting on correlated porous media. *J Phys D*. 1998;31(20):2861.
86. Sandhu J, Bansal H, Takhar PS. Experimental measurement of physical pressure in foods during frying. *J Food Eng*. 2013;115(2):272–277.
87. Gauglitz PA, Stlaurent CM, Radke CJ. An experimental investigation of gas-bubble breakup in constricted square capillaries. *J Petrol Technol*. 1987;39(9):1137–1146.
88. Unsal E, Mason G, Morrow NR, Ruth DW. Bubble snap-off and capillary-back pressure during counter-current spontaneous imbibition into model pores. *Langmuir*. 2009;25(6):3387–3395.
89. Fries N, Dreyer M. The transition from inertial to viscous flow in capillary rise. *J Colloid Interface Sci*. 2008;327(1):125–128.
90. Sánchez S, Méndez F, Bautista O. Capillary rise in a circular tube with interfacial condensation process. *Int J Therm Sci*. 2011;50(12):2422–2429.
91. Quéré D. Inertial capillarity. *Europhys Lett*. 1997;39(5):533–538.
92. Reeve RM. A review of cellular structure, starch, and texture qualities of processed potatoes. *Econ Bot*. 1967;21(4):294–308.
93. Konstankiewicz K, Czachor H, Gancarz M, Krol A, Pawlak K, Zdunek A. Cell structural parameters of potato tuber tissue. *Int Agrophys*. 2002;16(2):119–127.
94. Stanley DW, Tung MA. Microstructure of food and its relation to texture. In: DeMan JM, editor. *Rheology and Texture in Food Quality*. Westport: Avi Publishing Company, 1976:28–78.
95. Fedec P, Ooraikul B, Hadziyev D. Microstructure of raw and granulated potatoes. *Can Inst Food Sci Technol J*. 1977;10(4):295–306.
96. Pinthus EJ, Saguy IS. Initial interfacial-tension and oil uptake by deep-fat fried foods. *J Food Sci*. 1994;59(4):804–807.
97. Quinchia LA, Delgado MA, Valencia C, Franco JM, Gallegos C. Viscosity modification of high-oleic sunflower oil with polymeric additives for the design of new biolubricant formulations. *Environ Sci Technol*. 2009;43(6):2060–2065.
98. He D-B, Xu FEI, Hua T-C, Song X-Y. Oil absorption mechanism of fried food during cooling process. *J Food Process Eng*. 2013;36(4):412–417.
99. Pesse AV, Warrier GR, Dhir VK. An experimental study of the gas entrapment process in closed-end microchannels. *Int J Heat Mass Transfer*. 2005;48(25–26):5150–5165.
100. Dawson G, Lee S, Juel A. The trapping and release of bubbles from a linear pore. *J Fluid Mech*. 2013;722:437–460.
101. Unsal E, Mason G, Morrow NR, Ruth DW. Co-current and counter-current imbibition in independent tubes of non-axisymmetric geometry. *J Colloid Interface Sci*. 2007;306(1):105–117.
102. Unsal E, Mason G, Ruth DW, Morrow NR. Co- and counter-current spontaneous imbibition into groups of capillary tubes with lateral connections permitting cross-flow. *J Colloid Interface Sci*. 2007;315(1):200–209.

103. Hahn GJ, Shapiro SS. *Statistical Models in Engineering*. New York: Wiley, 1994.
104. Redner S. *A Guide to First-Passage Processes*. Cambridge: Cambridge University Press, 2001.
105. Opplestrup T, Bulatov VV, Gilmer GH, Kalos MH, Sadigh B. First-passage Monte Carlo Algorithm: diffusion without all the hops. *Phys Rev Lett*. 2006;97(23):230602.
106. Gibson LJ. The hierarchical structure and mechanics of plant materials. *J Roy Soc Interface*. 2012;9(76):2749–2766.
107. Karayiannis NC, Mavrantzas VG, Theodorou DN. Diffusion of small molecules in disordered media: study of the effect of kinetic and spatial heterogeneities. *Chem Eng Sci*. 2001;56(8): 2789–2801.
108. Kahng B, Redner S. Scaling of the first-passage time and the survival probability on exact and quasi-exact self-similar structures. *J Phys A*. 1989;22(7):887–902.
109. Sun D-W, Li B. Microstructural change of potato tissues frozen by ultrasound-assisted immersion freezing. *J Food Eng*. 2003;57(4):337–345.
110. Yamsaengsung R, Moreira RG. Modeling the transport phenomena and structural changes during deep fat frying—Part II: model solution & validation. *J Food Eng*. 2002;53(1):11–25.
111. Prat M. Recent advances in pore-scale models for drying of porous media. *Chem Eng J*. 2002;86(1–2):153–164.

Manuscript received Sep. 18, 2014, and revision received Feb. 17, 2015.